

## Journal Pre-proof

Ballistic impact response of elastomer-retrofitted corrugated core sandwich panels

Xin Wang , Zengshen Yue , Xiang Xu , Zhongnan Zhao ,  
Haibo Ji , Manyao Zhu , Pengfei Wang , Qiancheng Zhang ,  
Tian Jian Lu

PII: S0734-743X(23)00056-8  
DOI: <https://doi.org/10.1016/j.ijimpeng.2023.104545>  
Reference: IE 104545



To appear in: *International Journal of Impact Engineering*

Received date: 9 June 2022  
Revised date: 2 February 2023  
Accepted date: 10 February 2023

Please cite this article as: Xin Wang , Zengshen Yue , Xiang Xu , Zhongnan Zhao , Haibo Ji , Manyao Zhu , Pengfei Wang , Qiancheng Zhang , Tian Jian Lu , Ballistic impact response of elastomer-retrofitted corrugated core sandwich panels, *International Journal of Impact Engineering* (2023), doi: <https://doi.org/10.1016/j.ijimpeng.2023.104545>

This is a PDF file of an article that has undergone enhancements after acceptance, such as the addition of a cover page and metadata, and formatting for readability, but it is not yet the definitive version of record. This version will undergo additional copyediting, typesetting and review before it is published in its final form, but we are providing this version to give early visibility of the article. Please note that, during the production process, errors may be discovered which could affect the content, and all legal disclaimers that apply to the journal pertain.

© 2023 Published by Elsevier Ltd.

**Highlights**

- The concept of using polyurea coating to enhance ballistic performance of metallic corrugated core sandwich construction is proposed.
- Deformation and failure mechanisms of sandwich panels with/without polyurea reinforcing are elucidated.
- A finite element model based on the rate-dependent constitutive relation of polyurea works well to predict the ballistic impact response.
- Key factors affecting the effectiveness of polyurea in mitigating high-velocity projectile impact are analyzed.

**Ballistic impact response of elastomer-retrofitted corrugated core sandwich panels**

Xin Wang<sup>a,b</sup>, Zengshen Yue<sup>a</sup>, Xiang Xu<sup>c</sup>, Zhongnan Zhao<sup>f</sup>, Haibo Ji<sup>c,d</sup>, Manyao Zhu<sup>c,d</sup>,  
Pengfei Wang<sup>b</sup>, Qiancheng Zhang<sup>a\*</sup>, Tian Jian Lu<sup>c,d\*</sup>

<sup>a</sup>State Key Laboratory for Strength and Vibration of Mechanical Structures,

Xi'an Jiaotong University, Xi'an 710049, China

<sup>b</sup>Advanced Materials and Energy Center,

China Academy of Aerospace Science and Innovation, Beijing 100176, China

<sup>c</sup>State Key Laboratory of Mechanics and Control of Mechanical Structures,

Nanjing University of Aeronautics and Astronautics, Nanjing 210016, China

<sup>d</sup>MIIT Key Laboratory of Multifunctional Lightweight Materials and Structures (MLMS),

Nanjing University of Aeronautics and Astronautics, Nanjing 210016, China

<sup>e</sup>School of Engineering, Anhui Agriculture University, Hefei 230036, China

<sup>f</sup>Northwest Institute of Nuclear Technology, Xi'an 710024, China

\*Corresponding authors: tjlu@nuaa.edu.cn (TJL), zqc111999@xjtu.edu.cn (QCZ)

**Abstract:**

The ballistic impact resistance of metallic corrugated sandwich panels retrofitted with elastomeric coating (polyurea) is investigated through combined experimental and numerical efforts. Dynamic penetration process, failure mechanisms, ballistic limit velocity, and perforation energy threshold of polyurea-coated sandwich panels are firstly elucidated via experiments and then compared with those of non-coated sandwich panels. Subsequently, based upon a user-defined compressible model of polyurea, three-dimensional finite element (FE) simulations of both non-coated and coated sandwich panels are carried out to analyze the ballistic impact response, interrogate the energy absorption mechanisms, and assess the influence of coating position/thickness and projectile rigidity on ballistic performance. Excellent agreement between experimental measurements and numerical predictions is achieved. It is demonstrated that the presence of a sufficiently thick (e.g., ~15 mm) impact-side elastomeric coating helps to curtail the kinetic energy of flat-ended projectiles, thus enhancing the penetration resistance considerably. The use of a thicker and impact-side coating is favored owing to its superior energy absorption capability. It is also ascertained that the effectiveness of polyurea coating in resisting rigid,

flat-ended projectiles is much more remarkable relative to deformable, conical ones. Further, retrofitting an all-metallic sandwich panel with elastomeric coating broadens its multifunctionality significantly, enabling it to simultaneously carry structural loads, mitigate impact and blast loadings, and resist projectile penetration, at a minimal increase in fabrication cost and structural mass. The insights of this study provide a potential new avenue for enhancing the ballistic impact resistance as well as multifunctional attributes of all-metallic sandwich construction.

**Keywords:** ballistic resistance; sandwich panel; elastomeric coating; corrugated core; energy absorption

## 1. Introduction

Naval vessels play an essential role in modern naval warfare as sustained operation platforms where navies carry out a variety of military missions [1–3]. With ever-rising strike precision and charge volume, anti-ship weaponry has emerged as one of the most lethal threats to both surfaces and submerged vessels [4]. For instance, large surface vessels are heavily threatened by semi-armor piercing anti-ship missiles whose strike location is usually above the waterline [5]. With great kinetic energy, the missiles (with an impact velocity of  $\sim 10^2$  m·s<sup>-1</sup> and warhead mass of  $\sim 10^2$  kg) are able to penetrate broadside plates and then explode inside cabins, thus leading to catastrophic structural damage and loss of human lives [6]. In general, the destruction from semi-armor piercing missiles can be briefly attributed to the following aspects [7]: (i) intact missiles pierce the hull with severe perforation, around which large plastic deformation and ductile fracture of the target occur [8]; (ii) high-temperature/pressure detonation products together with initial shock wave and subsequent quasi-static pressure exacerbate the structural damage with a larger affected area [9]; (iii) fragmentation of warhead casing and damaged hull structures during explosion generates high-velocity fragment clusters, which impart additive and cumulative damage on the target [10]; (iv) fires induced by detonation products weaken the hull structures and enable the injury/death of human lives [11]. Consequently, to improve the survivability of large surface vessels, it is necessary to endow their hull structures with superior blast resistance, ballistic performance, and structural efficiency [12].

The last two decades have witnessed a rapid proliferation of all-metallic corrugated sandwich

structures in various engineering fields, especially for marine constructions. Due to their high structural efficiency and outstanding mitigation on impact loading (e.g., explosion, collision, grounding, etc.), corrugated sandwich structures are substantially supplanting conventional monolithic and stiffened counterparts as a technically compliant solution to ship hull design [13]. For typical instance, the US Navy's most advanced surface combatant - USS Zumwalt (also named DDG-1000) has been equipped with laser-welded corrugated sandwich panels as hull components (e.g., berms and personnel safety barrier panels) [14]. Thus far, there have been plenty of research efforts devoted to elucidating the dynamic response of metallic corrugated sandwiches to shock loading from different sources, such as air blast [15], underwater blast [16], soil blast [17], foam projectile impact [18], and the like [19–24]. To meliorate their vulnerability against high-intensity shock, novel tactics of hybrid sandwich cores have also been proposed and implemented by filling or in-situ synthesizing certain materials into the interstices of corrugated plates, including foam [25], honeycomb [26], sand [27], and liquid [28]. Nevertheless, this strategy appears to be less effective in dealing with structures experiencing large deflection, for the corrugated core contributes less to membrane stretching of a sandwich panel relative to its thin metallic face sheets [27,28].

Additionally, given that explosion events in naval vessels are usually accompanied by high-velocity fragments, in-depth insights into the ballistic performance of corrugated sandwiches are also of utmost importance [29–31]. In contrast to shock loading, the structural response to high-velocity projectile impact is more localized and typically independent of boundary conditions, thus leading to more concentrated dissipation of projectile kinetic energy at the impact site [32]. Previous studies have revealed that the ballistic resistance of a sandwich panel with either pyramidal lattice or corrugated core is indistinguishable from, or even worse than, that of its solid (monolithic) counterpart having the same areal density [33–35]. Fortunately, although it is difficult for low-density corrugated cores to deflect incident projectiles, the spacious core voids allow for embedding ballistic resistant materials, including polymer [33], ceramic [35], concrete [36], sand [37], and so on. The mechanism is that the incorporation of such core fillers helps decelerate and erode projectiles, thus strengthening the ballistic performance of the hybrid core [29]; further, the discrete distribution of fillers in the corrugated core enables withstanding multi-hits of projectiles [35]. Nonetheless, a metallic corrugated core filled with stiff materials (e.g., ceramic and sand) for

enhanced penetration resistance can not be sufficiently crushed, thus deteriorating its originally excellent energy absorption capacity against blast loading. In summary, designing ultralightweight, structural load bearing corrugated core sandwiches against simultaneous blast and ballistic loading remains a tough task to be addressed.

Emerged in the 1980s, polyurea elastomer is an environmentally-friendly copolymer formed by condensation polymerization of isocyanates and amines [38]. Based upon the spray-cast fabrication technique, polyurea can be applied to virtually any hard substrate, easily and rapidly. Recently, retrofitting a metallic substrate with elastomeric coating has been extensively implemented as a practical approach to improve its survivability, especially when subjected to intense blast and ballistic loadings [39]. Adding a polyurea layer was found to have a positive effect on the dynamic response of steel plates to impulsive loading in terms of structural damage and energy absorption, due to delayed onset of necking in the steel [40]; meanwhile, the effects of coating thickness, coating position, and interfacial strength on the level of benefit were also testified [41,42]. Selection of polyurea coating was also vital, as polyurea with high strength but low ductility fractures at small strains and spall off, thereby curtailing its contribution to protection [43]. On the other hand, it was demonstrated that polyurea coating with appropriate thickness increases the ballistic limit and energy absorption characteristics of metal targets substantially [44,45]; the influences of substrate hardness, substrate thickness, and coating thickness on the ballistic performance were investigated as well [46]. Similar conclusions were reached in various ballistic impact test scenarios regarding the shape of penetrator [47–49]. In addition to remarkable blast/ballistic mitigation, the high durability of polyurea coating facilitates long-term stable service in the marine environment due to its excellent adhesion to metals, impermeability to moisture, and resilience to corrosion/abrasion/temperature [50–52].

Motivated by the above literature review, the present study proposes a novel ballistic-mitigating corrugated sandwich construction by retrofitting its metal face sheets with polyurea reinforcing layers. With reference to the authors' past work [53–56], it has been demonstrated that the existence of polyurea coating significantly improves the passive vibration attenuation and blast resistance of corrugated sandwich panels. However, little is known about the ballistic resistance of such sandwich construction. Therefore, based upon systematic experimental

testing and finite element (FE) simulation, the current study aims to reveal and compare the ballistic limit and energy absorption characteristics of sandwich structures retrofitted with and without polyurea coating. Underlying physical mechanisms by which the coating achieves its mitigation effect on high-velocity projectile impact are also interrogated.

## 2. Experimental details

### 2.1. Scope of experimental study

Via a two-stage light-gas gun, flat-ended cylindrical projectiles are fired to dynamically strike edge-clamped corrugated sandwich panels with and without polyurea coating. The primary aims of the investigation include: (i) compare the ballistic limit and energy absorption characteristics of sandwich panels retrofitted with and without elastomeric coating, (ii) interrogate the deformation/failure mechanisms of both non-coated and coated panels, and (iii) verify the fidelity of subsequent FE simulations on ballistic penetration.

### 2.2. Geometric configuration

**Figure 1** exhibits the geometric configuration and representative volume element (RVE) of a square corrugated sandwich panel investigated in the present study, which comprises two identical face sheets and a trapezoidal corrugated core. A global coordinate system  $(x, y, z)$  is selected, where  $x$ ,  $y$ , and  $z$ -axis denote the longitudinal, transverse, and out-of-panel direction of the corrugated core, respectively. Key geometric parameters include: length  $L$  and height  $H$  of sandwich panel; face sheet thickness  $t_f$ ; core height  $H_c$ ; length  $l_c$ , thickness  $t_c$ , and inclination angle  $\theta$  of corrugation member; corrugation platform length  $l_p$ ; PMMA insert length  $L_b$ ; and bolt hole diameter  $d_b$ . **Table 1** summarizes geometric parameters of metallic corrugated sandwich panels to be fabricated.

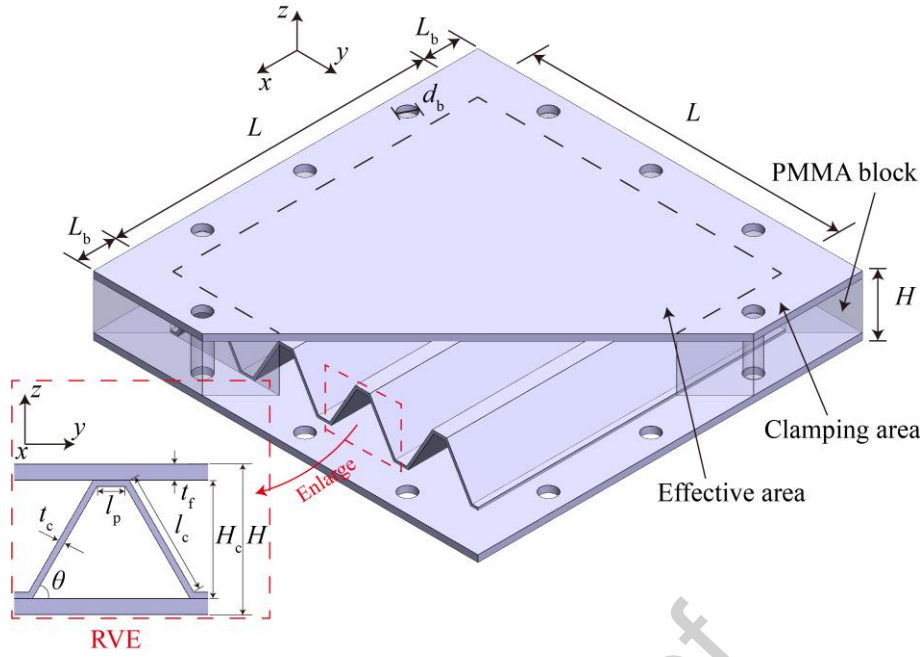


**Fig. 1.** Geometric schematic of corrugated sandwich panel to be fabricated.

**Table 1.** Geometric parameters of corrugated sandwich panels studied (unit: mm).

$L$	$t_f$	$t_c$	$l_c$	$l_p$	$\theta$	$L_b$	$d_b$
120	2.5	1	20	5	$60^\circ$	30	6.4

### 2.3. Manufacture procedures

**Figure 2** presents both non-coated and coated corrugated sandwich panels fabricated and tested in the current work. All-metallic corrugated sandwich panels are manufactured from AISI 304 stainless steel sheets (supplied by Shanghai Haocheng Co., Ltd.). Precise assembly of face sheets and corrugated core is achieved via vacuum brazing, with details demonstrated in the references [27,28]. Nickel-based alloy powder BNi-7 (supplied by Changsha Tianjiu Co., Ltd.) is used as the solder, with a brazing temperature of  $1040^\circ\text{C}$  and vacuum degree of  $\sim 10^{-2}$  Pa adopted. A uniform retrofit of bare sandwich specimens is carried out with the highly stretchable polyurea Qtech-420 (supplied by Qingdao Shamu Co., Ltd.). The mass density of Qtech-420 is measured to be  $950 \text{ kg/m}^3$ , and its dynamic mechanical properties are detailed in **Fig. 12**. With the aid of pre-applied primer, the polyurea coating is able to adhere to metal face sheets. To ensure the superior mechanical properties of polyurea, after spraying, all test samples are preserved at room temperature for two weeks. Due to the present manual spraying operation, the coating thickness is measured to be  $\sim 15$  mm, with a rough



error of  $\pm 0.5$  mm.

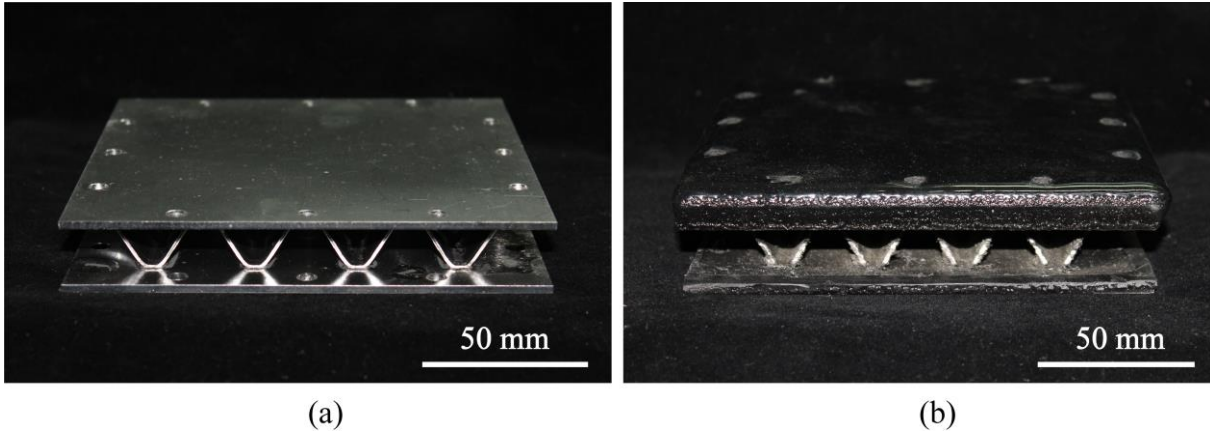


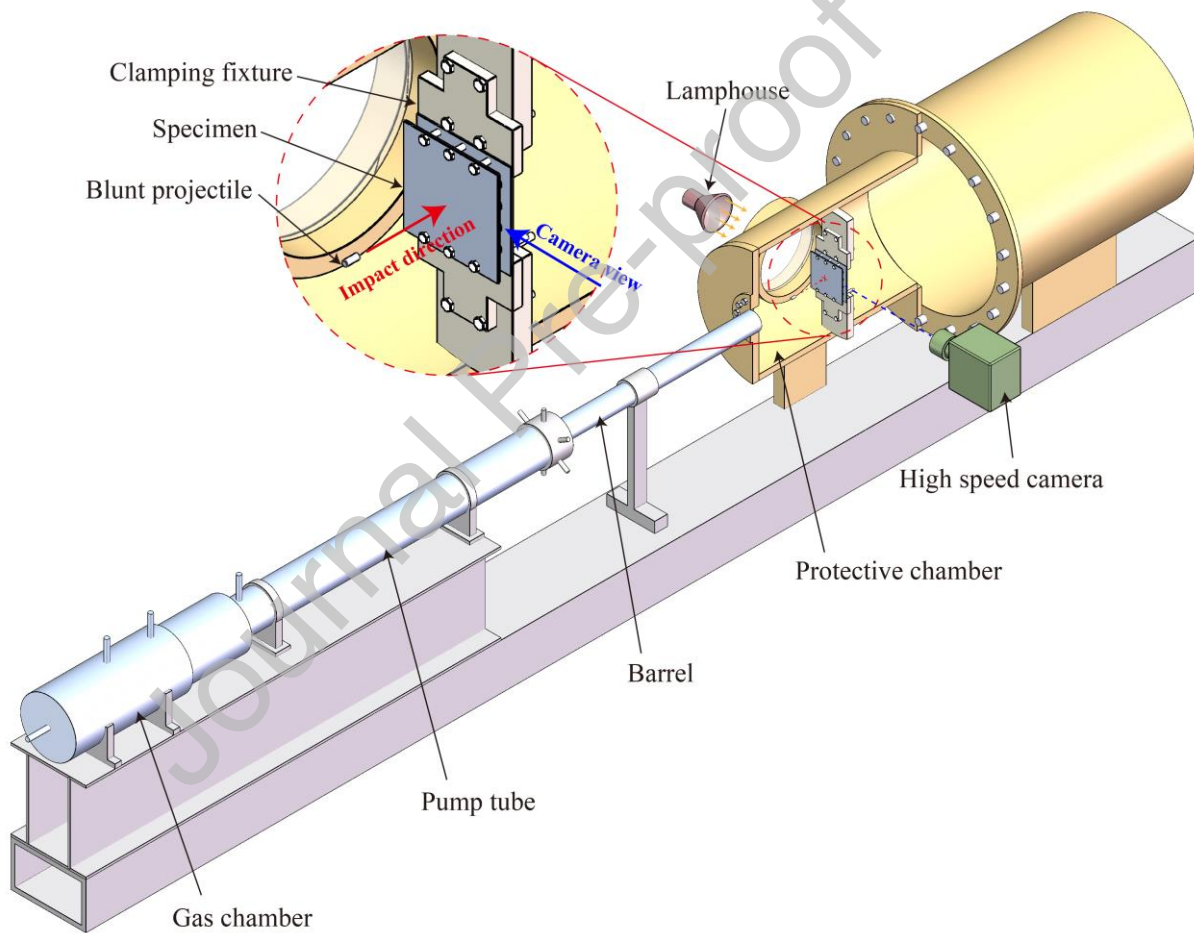
**Fig. 2.** As-fabricated corrugated sandwich panels: (a) non-coated and (b) polyurea-coated.

#### 2.4. Ballistic impact test protocol

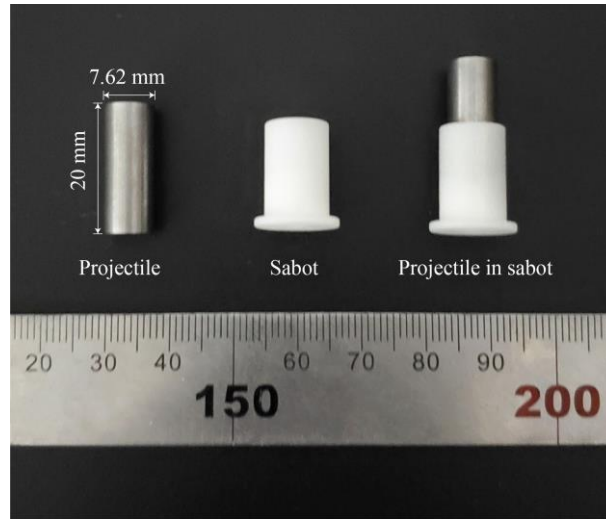
As listed in **Table 2**, ballistic penetration of non-coated sandwich panels is investigated for projectile impact velocities varying in the range of  $449 \leq v_i \leq 718$  m·s<sup>-1</sup>, while that of impact-side coated sandwich panels is studied in an impact velocity range of  $526 \leq v_i \leq 706$  m·s<sup>-1</sup>. **Figure 3** shows the two-stage light-gas gun system used for ballistic tests, which encompasses a gas chamber, a barrel, and a protective chamber. As shown in **Fig. 4**, flat-ended projectiles made of AISI 4340 steel (35 HRC hardness) are employed, each with a diameter of 7.62 mm, a height of 20 mm, and a mass of 7.14 g. For each test, the projectile is fixed in a polyethylene sabot with an obturator and then inserted into the barrel. Note that the sabot should be as lightweight as possible to avoid undesirable pitch and yaw of the projectile. Due to the low mass (~0.8 g) and low strength (~10 MPa) of the sabot, its influence on the ballistic impact response of sandwich specimens is considered negligible.

All test specimens, with an effective area of 120 × 120 mm, are mounted in a nearly rigid fixture (made of high-strength structural steel Strenx<sup>®</sup> 960) using six M6 bolts along both top and bottom edges; see the enlarged viewpoint of **Fig. 3**. To fasten the clamping boundary, two drilled PMMA blocks are also inserted and glued around the clamping edges of the specimen using double-sided acrylic foam adhesive tapes (3M VHB<sup>™</sup> 5608). It has been established that the ballistic performance of a lattice core sandwich panel significantly depends on how the incident penetrator interacts with its core [34]. For consistency, the muzzle is carefully aligned with the centre of an edge-clamped sandwich panel to achieve joint impact on the brazing platform of the

corrugated core with zero obliquity (as shown in **Table 2**). Note that the influence of impact location is numerically discussed in **Appendix**. The dynamic penetration process of each specimen, as well as the corresponding projectile trajectory, are recorded using a high-speed camera (I-SPEED 713, IX), with an inter-frame time of  $20 \mu\text{s}$ , exposure time of  $2 \mu\text{s}$ , and image resolution of  $366 \times 366$  pix, respectively. Both the impact and residual velocities at each test are calculated using commercially available motion analysis code (ProAnalyst, Xcitex), with a precision of  $\pm 3 \cdot \text{m} \cdot \text{s}^{-1}$ . After the impact, a postmortem evaluation is undertaken on each test specimen, with/without coating, to analyze its deformation/failure mechanisms.



**Fig. 3.** Schematic of a two-stage light-gas gun system for projectile penetration test.

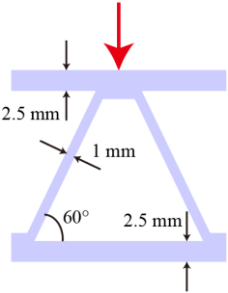
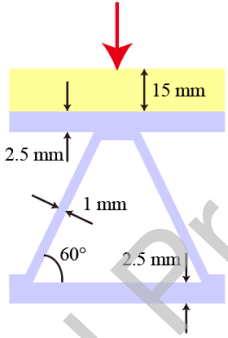


**Fig. 4.** Flat-ended projectile and polyethene sabot.

### 3. Experimental results

This section details experimental observations in three aspects: (i) dynamic penetration process via recorded high-speed photographs, (ii) deformation and failure modes via post-test examination on deformed sandwich panels, and (iii) ballistic impact resistance via two quantitative parameters - ballistic limit velocity and perforation energy threshold. Experimental results are summarized in **Table 2**. For clarity, let the face sheet to be impacted be denoted as the impact face and the other one as the rear face, and let  $m_s$ ,  $v_i$  and  $v_r$  denote the sample mass, impact velocity, and residual velocity of each test, respectively. Further, three abbreviations, i.e., **S**, **PS**, and **SP**, are adopted to represent separately non-coated, impact-side coated, and rear-side coated corrugated sandwich panels.

**Table 2.** Experimental summary of ballistic impact tests.

Specimen No.	Configuration	$m_s$ (g)	$v_i$ (m·s <sup>-1</sup> )	$v_r$ (m·s <sup>-1</sup> )
S-1		1049.72	449	0
S-2		1045.63	503	109
S-3		1055.05	516	136
S-4		1052.29	552	176
S-5		1051.85	662	352
S-6		1061.32	718	422
PS-1			1351.76	526
PS-2	1365.61		643	243
PS-3	1355.48		657	234
PS-4	1361.03		706	340

 304 stainless steel; 
  Polyurea elastomer; 
  Impact direction

### 3.1. Dynamic penetration process

First and foremost, the definition of penetration needs clarification to avoid any conflict. Recall a classical note on the mechanics of projectile penetration by Backman and Goldsmith [57]. The term “penetration” is defined as the entry of a penetrator into any region of a target, thus leading to three possible regimes: (i) perforation, which means the penetrator passes through the target, (ii) embedment, which indicates the penetrator is arrested during contact with the target, and (iii) ricochet, which means the penetrator is deflected from the target without being stopped or perforating. In practice, how each regime would occur is generally related to material properties, geometric features, and impact velocity. Following such a definition, one conclusion can be drawn from experimental observations: both perforation and embedment happen in the present ballistic test

set, except for ricochet, as detailed below.

As depicted in **Figs. 5 ~ 6**, the dynamic penetration processes of non-coated specimens (**S-1** and **S-6**) at two selected impact velocities are manifested via a sequence of high-speed photographs, with the time labelled on each image calculated with reference to the instant of impact commencement. At a lower impact velocity ( $v_i = 449 \text{ m}\cdot\text{s}^{-1}$ ), the projectile perforates both the impact face and core platform at  $t \approx 41 \text{ }\mu\text{s}$ , interacts with the rear face at  $t \approx 61 \text{ }\mu\text{s}$ , and then is entirely arrested at  $t \approx 161 \text{ }\mu\text{s}$ . Since  $t \approx 81 \text{ }\mu\text{s}$ , the rear face suffers a significant out-of-plane deformation, initiated at the impact site and propagating to the clamped edge. At a higher impact velocity ( $v_i = 718 \text{ m}\cdot\text{s}^{-1}$ ), the penetrator pierces the impact face and core platform at  $t \approx 33 \text{ }\mu\text{s}$  and then passes through the rear face at  $t \approx 73 \text{ }\mu\text{s}$ . After  $t \approx 93 \text{ }\mu\text{s}$ , the eroded projectile accompanied with a dark cloud is emitted from the perforation, around which severe warping is observed. The cloud encompasses a large body of tiny fragments associated with the fracture of sandwich components and polymeric sabot as well as a small amount of dust from the gun barrel. In comparison, the polyurea-coated specimen **PS-4** exhibits a consistent penetration response, as shown in **Fig. 7**. That is, the free-flying projectile with an initial velocity of  $v_i = 706 \text{ m}\cdot\text{s}^{-1}$  perforates the polyurea coating, the impact face and core platform, and the rear face at  $t \approx 31, 51, \text{ and } 111 \text{ }\mu\text{s}$ , respectively.

Additionally, the high-speed images collected in **Figs. 5 ~ 7** reveal two facts: (i) each test sample is accurately positioned so that the projectile perfectly impacts its central region supported by a corrugation platform, and (ii) the sabot is brittle and well-designed, thereby enabling normal incidence of each projectile, without apparent pitch and yaw. For each test, a bright light appears in the corrugated core after the projectile completely perforates the impact face and begins to interact with the rear face (e.g., see the photo at time  $t = 71 \text{ }\mu\text{s}$  in **Fig. 7**). Consistent with a previous study [34], this interesting phenomenon is attributed to the shock wave that passes through the impact face, reflects from the rear face, and interacts with the corrugated core, thereby causing a dramatic pressure rise; further, the high pressure leads to ionization of the air trapped between the impact and rear faces; finally, the air ionization highlights itself in the high-speed image as bright light.

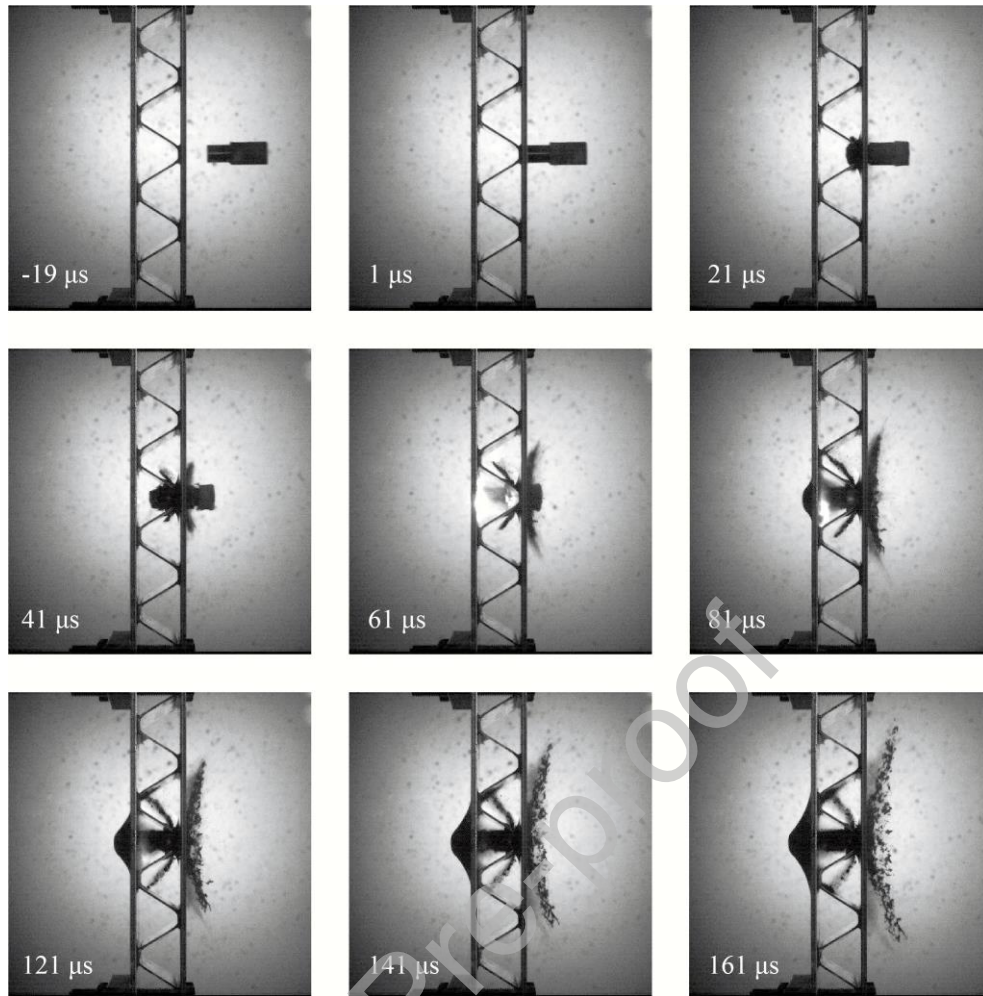


**Fig. 5.** High-speed images of non-coated specimen S-1 impacted by a flat-ended projectile at  $v_i = 449 \text{ m}\cdot\text{s}^{-1}$ .

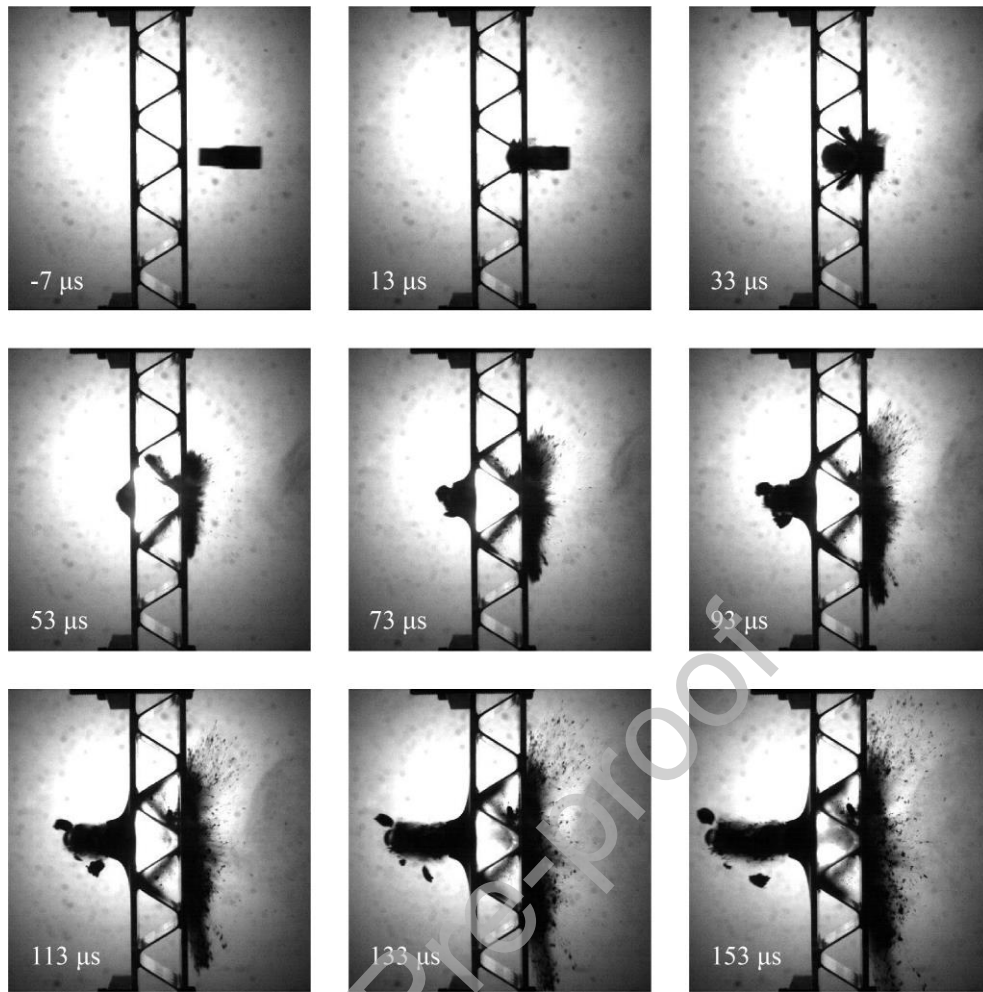


**Fig. 6.** High-speed images of non-coated specimen S-6 impacted by a flat-ended projectile at  $v_i = 718 \text{ m}\cdot\text{s}^{-1}$ .



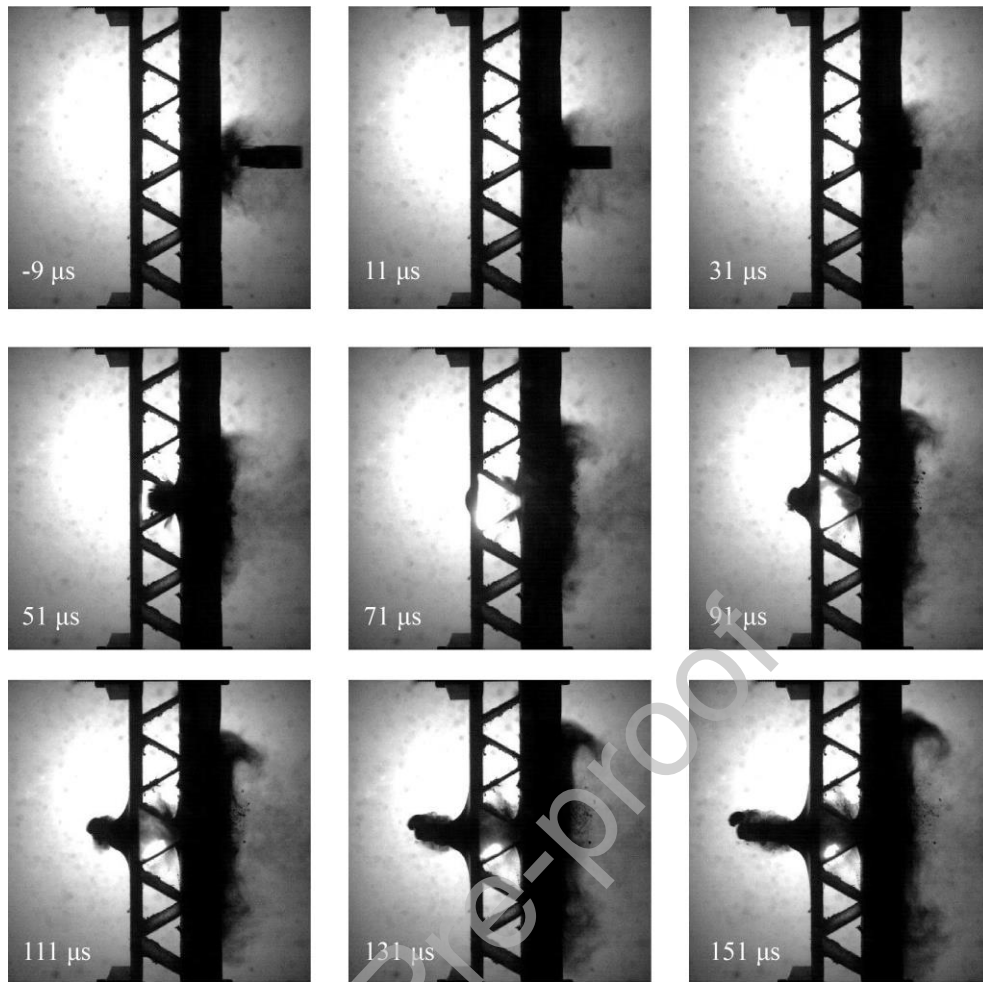


**Fig. 7.** High-speed images of polyurea-coated specimen **PS-4** impacted by a flat-ended projectile at  $v_i = 706 \text{ m}\cdot\text{s}^{-1}$ .

### 3.2. Failure mechanisms

The same compendium by Backman and Goldsmith [57] presents a comprehensive insight into the failure modes of a metal target under ballistic impact, which are usually encountered in cases where the projectile strength is in excess of that of the target. In general, for a metallic target, these failure modes can be classified into two regimes according to its ductility [58]. A low ductility target typically fails in the following modes: (i) spall fracture, which usually happens near the rear surface when the tensile stress there exceeds the tensile strength; (ii) plugging, which is caused by adiabatic softening and shear failure at the periphery of the projectile; (iii) radial fracture, due to the low tensile radial strength of the metal. On the other hand, a metallic target with high ductility exhibits totally different failure mechanisms: (i) petaling, induced by large bending deformation and subsequent fracture initiation at the impact site, where inhomogeneities or weaknesses exist. Regarding its rotational direction, a rearward petaling often occurs in thin targets while a frontal one



appears in thick plates; (ii) ductile hole enlargement, which is commonly observed in the impact events of thick targets and heavily dependent upon projectile nose shape and target thickness. Additionally, the non-perforating failure modes are classified as: (i) bulging, which exists in the projectile-target contact region and conforms to the projectile nose shape; (ii) dishing, which is caused by large bending deformation of the target, usually extending a considerable distance from the bulge. With reference to the above, this section interrogates the deformation and failure mechanisms of non-coated and coated sandwich specimens struck by flat-ended projectiles.

To start with, **Fig. 8** presents the typical failure modes of non-coated corrugated sandwich panels impacted at selected velocities. For all the samples studied, the penetration of impact face is dominated by plugging. Due to the adiabatic softening effect, a circumferential crack is more likely to be formed at the impact site than a radial crack. Correspondingly, the metallic face sheet is entirely sheared off at the periphery of the penetrating projectile, resulting in a cylindrical plug ejected from the entry hole. The diameter of the entry hole in each sample is slightly less than 8 mm and is nearly the same as that of the projectile. No significant bending deformation or ductile hole enlargement is observed around the crater. By contrast, the rear face undergoes a more complicated failure process which is associated with the impact velocity. For specimen **S-1** impacted at a lower velocity ( $v_i = 449 \text{ m}\cdot\text{s}^{-1}$ ), the projectile is completely impeded by the rear face on which a non-perforating failure mode is observed. Marked by two red circles in **Fig. 8a**, bulging deformation happens within the projectile periphery, whereas dishing deformation caused by plastic bending and even stretching is observed outside the periphery. Next, consider specimen **S-3** subjected to an increased impact velocity of  $v_i = 516 \text{ m}\cdot\text{s}^{-1}$ . Similar to previous studies [59,60], perforation of rear face is governed by a flipped-cover tearing mechanism (also called discing), as shown in **Fig. 8b**. This failure mode may be attributed to the following mechanisms: upon perforating both the impact face and core platform, the eroded projectile may interact with the rear face with a slight obliquity; then, a circumferential crack is more prone to occur at a particular location of the contact patch; subsequently, the marching projectile enables propagation of the initial crack, so that the slug within the projectile periphery also tears and flips forward along the same direction. For the last two specimens, **S-5** and **S-6**, which are impacted at higher impact

velocities ( $v_i = 662$  and  $718 \text{ m}\cdot\text{s}^{-1}$ , respectively), the rear faces of both fail with a petaling mechanism. As depicted in **Fig. 8c**, the rear face of **S-5** experiences a severe bending deformation, leading to the formation of four or five petals between which minor radial cracks exist. With the increase of impact velocity, the petals of **S-6** fracture with some debris owing to the growing role of shear deformation around the projectile periphery (**Fig. 8d**). For accuracy, the process of petal rupture captured by a high-speed photograph at time  $t = 113 \mu\text{s}$  is presented in **Fig. 6**.

Similar to uncoated specimens, **Fig. 9** displays representative deformation and failure modes of polyurea-coated corrugated sandwich panels impacted at various incidence velocities. Again, the ballistic impact response of impact faces is dominated by plugging. The failure of polyurea coating is governed by the so-called self-closing mechanism [61], which means that the entry hole of polyurea coating somewhat closes up after perforation. One convincing explanation is that, due to superior ductility and hyperelasticity, the elastomeric coating is able to withstand severe deformation during projectile penetration and recover rapidly after the exit of projectile. As shown in **Fig. 9**, with the increase of impact velocity, the crater of polyurea coating is enlarged but still smaller than the projectile. Such behaviour is also encountered in low-hardness polyurea subjected to ballistic impact [61], especially under the strike of conical-nosed projectiles. Note also that a previous study elucidated a superior efficacy of high-hardness polyurea to the low-hardness one [48]: the higher dissipation of impact energy is realized via large-scale brittle cracking/spalling and interfacial debonding. Under such conditions, the self-closing feature of polyurea coating is curtailed significantly. In contrast, failure mechanisms of the uncoated rear faces are associated with impact velocity, i.e., bulging and dishing (**PS-1**), flipped-cover tearing (**PS-2/PS-3**), and petaling (**PS-4**). Additionally, for all the samples, with or without polyurea coating, interfacial failure of brazing joints slightly occurs in the rear faces, owing to their extensive bending and stretching near the impact site.

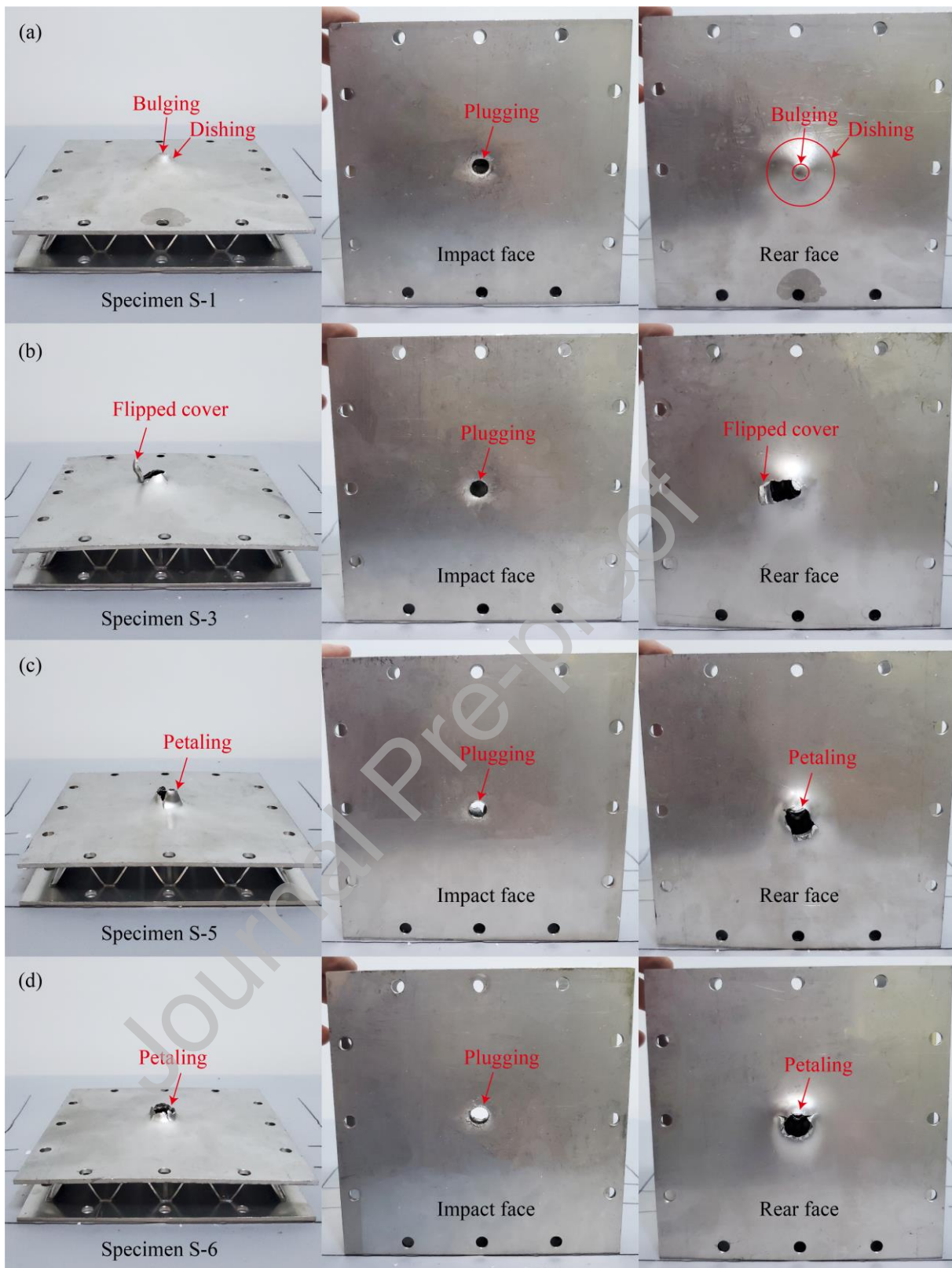


**Fig. 8.** Typical deformation/failure modes of non-coated sandwich specimens: (a) S-1, (b) S-3, (c) S-5, and (d) S-6.

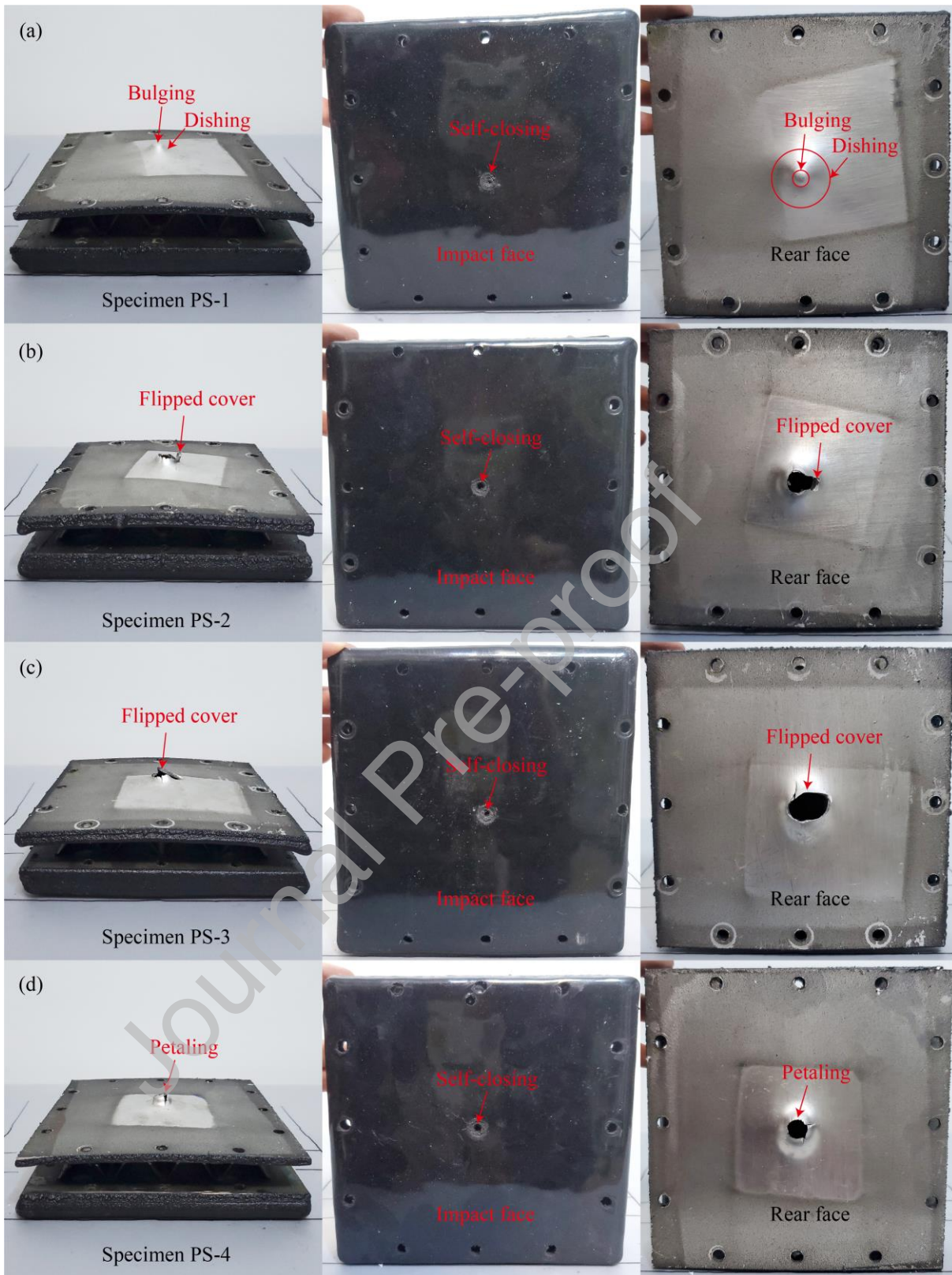


**Fig. 9.** Typical deformation/failure modes of sandwich specimens with polyurea-coated impact faces: (a) PS-1, (b) PS-2, (c) PS-3, and (d) PS-4.

### 3.3. Quantitative assessment

Two quantitative parameters are adopted to evaluate the ballistic performance of both coated and non-coated sandwich specimens: (i) ballistic limit velocity  $v_{bl}$ , defined as the impact velocity when the projectile is either stuck in the target or exits with a negligibly low velocity [62]; (ii) perforation energy threshold  $E_{pt}$ , defined as the projectile kinetic energy at ballistic limit [63]. Herein, the Lambert-Jonas (LJ) formula is applied to fit the residual velocity curve to quantify the ballistic limit velocity, as [64,65]:

$$v_r = \begin{cases} 0 & 0 \leq v_i \leq v_{bl} \\ \alpha (v_i^\beta - v_{bl}^\beta)^{1/\beta} & v_i > v_{bl} \end{cases} \quad (1)$$

where  $\alpha$  and  $\beta$  are two model parameters to be calibrated. Then, the perforation energy threshold can be calculated as follows:

$$E_{pt} = \frac{1}{2} m_p v_{bl}^2 \quad (2)$$

where  $m_p$  is the projectile mass. Note that all the fitting procedures are conducted using the commercially available software Wolfram Mathematica v12.0, in which the optimal parameters are attained by employing the Levenberg-Marquardt algorithm.

For both non-coated and coated panels, **Fig. 10** plots the residual velocity of projectile as a function of initial impact velocity. Near the ballistic limit, the residual velocity drops to zero sharply. **Table 3** presents the optimal Lambert-Jonas equation constants for non-coated and coated specimens. It is ascertained that, with the aid of impact-side polyurea coating, the ballistic limit of the metallic corrugated sandwich panel is increased from 470 to 530  $\text{m}\cdot\text{s}^{-1}$  by about 11.3%. Additionally, the perforation energy threshold is raised from 789 to 1003 J by around 27.1%, suggesting a substantial enhancement of ballistic performance. It should be noted that the superior ballistic performance also leads to around a 29% increase in the structural mass (**Table 2**). In the next section, to extend the limited experimental data acquisition, a more sophisticated estimation of the efficacy of polyurea coating is carried out via FE simulations.



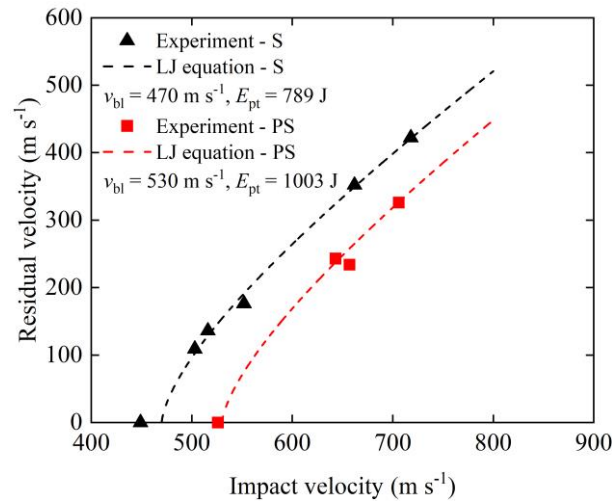


**Fig. 10.** Residual velocity plotted as a function of initial impact velocity for both non-coated (S) and impact-side coated (PS) sandwich panels.

**Table 3.** Optimal Lambert-Jonas model constants for non-coated and coated corrugated sandwich panels.

Target	$\alpha$	$\beta$	$v_{bl}$ (m·s <sup>-1</sup> )
Non-coated panel	0.971	1.497	470
Impact-side coated panel	0.966	1.459	530

#### 4. Finite element calculations

The commercially available FE code ABAQUS v2020 is utilized to conduct numerical simulations on the ballistic impact response of both non-coated and coated corrugated sandwich panels. In addition to experimental observations detailed in **Section 3**, valuable results not available from experiments are showcased, including energy absorption characteristics of the substructures constituting the sandwich, either coated or non-coated. These clues enable a more elaborated elucidation of physical mechanisms underpinning the enhanced ballistic resistance of a coated sandwich. Also, primary factors affecting ballistic resistance are discussed.

##### 4.1. Model description

For balanced computational cost and accuracy, FE models of one-quarter corrugated sandwich panels retrofitted with and without polyurea coating are adopted, with two symmetric boundary conditions applied, as shown in **Fig. 11**. For each panel, the impact/rear face, corrugated core, flat-ended projectile, and polyurea coating are modelled using eight-node brick elements with

reduced integration (C3D8R in ABAQUS nomenclature). The mesh size in the sandwich central zone (about 10 mm long,  $\sim 2.6$  times the projectile radius) is 0.1 mm, as recommended by Mohr et al. [66,67]. Equally, the fine meshing of 0.1 mm is also selected for the projectile. By contrast, the rest of each substructure is discretized with a gradient elevation in grid size, from 0.5 to 2.5 mm towards panel edge. In sum, the total element numbers of non-coated and coated specimens are respectively 1709460 and 4409460. Following experimental observation, the corrugated core is assumed to be perfectly bonded with face sheets using a tie contact algorithm, and the same contact option is set for the face sheet-polyurea coating interface. More importantly, the tangential frictionless interaction between the substructure and projectile is modelled using a general contact option instead of a surface-to-surface one, for the latter only accounts for the contact of elements existing on two surfaces - if surface elements are deleted, the inner elements are unable to interact with each other anymore. Additionally, relaxed stiffness-based suppression of hourglass energy is activated to ensure the energy balance of the present FE simulations.

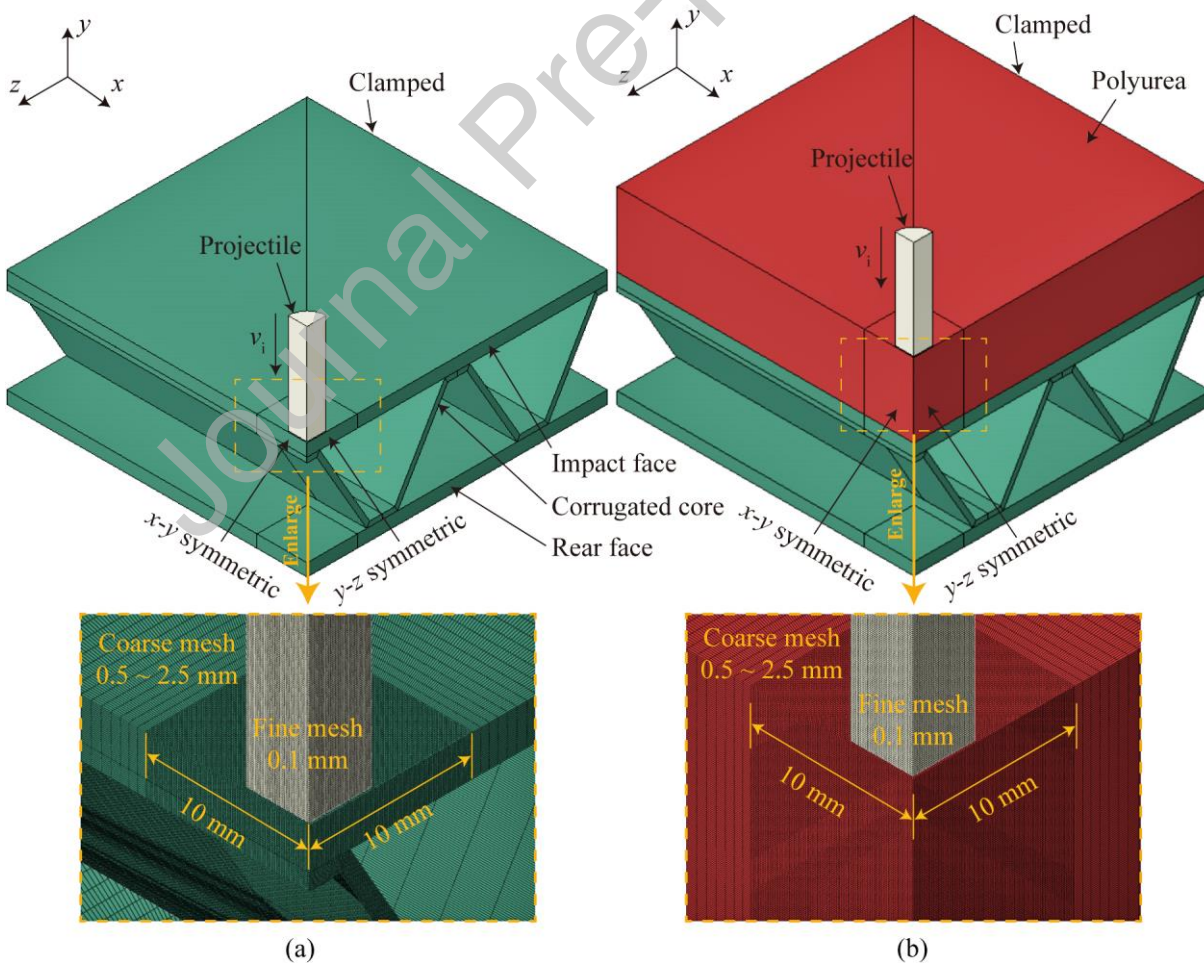


**Fig. 11.** Numerical simulation models for (a) non-coated and (b) impact-side coated specimens.

## 4.2. Constitutive relation

### 4.2.1. Steel

An elastoplastic constitutive equation is invoked to describe both 304 stainless steel (sandwich panel) and 4340 steel (flat-ended projectile). Specifically, the classical Johnson-Cook (JC) plasticity formula is used to model isotropic strain hardening, as:

$$\sigma_{\text{eq}}(\varepsilon_{\text{pl}}, \dot{\varepsilon}_{\text{pl}}, T) = (A + B\varepsilon_{\text{pl}}^n) \left[ 1 + C \ln \left( \frac{\dot{\varepsilon}_{\text{pl}}}{\dot{\varepsilon}_0} \right) \right] \left[ 1 - \left( \frac{T - T_r}{T_m - T_r} \right)^m \right] \quad (3)$$

where  $A$ ,  $B$ ,  $n$ ,  $C$  and  $m$  are model constants,  $\sigma_{\text{eq}}$  is equivalent plastic stress,  $\varepsilon_{\text{pl}}$  and  $\dot{\varepsilon}_{\text{pl}}$  are equivalent plastic strain and strain rate,  $\dot{\varepsilon}_0$  is reference strain rate,  $T_r$  is room temperature, and  $T_m$  is melting temperature. In addition to plasticity, the JC fracture criterion is employed to characterize ductile fracture of steel, with the effects of stress state (triaxiality), strain rate, and temperature on fracture strain all accounted for. Theoretically, a damage indicator to an element is defined as:

$$D = \sum \frac{\Delta \varepsilon_{\text{pl}}}{\varepsilon_f} \quad (4)$$

where  $\Delta \varepsilon_{\text{pl}}$  is the equivalent plastic strain accumulated over a time increment, and  $\varepsilon_f$  is the equivalent plastic strain to fracture. An element fractures when the indicator  $D = 1$ . The mathematical expression of  $\varepsilon_f$  is:

$$\varepsilon_f(\sigma^*, \dot{\varepsilon}_{\text{pl}}, T) = (D_1 + D_2 e^{D_3 \sigma^*}) \left[ 1 + D_4 \ln \left( \frac{\dot{\varepsilon}_{\text{pl}}}{\dot{\varepsilon}_0} \right) \right] \left[ 1 - \left( \frac{T - T_r}{T_m - T_r} \right)^{D_5} \right] \quad (5)$$

where  $D_1$ ,  $D_2$ ,  $D_3$ ,  $D_4$  and  $D_5$  are model parameters,  $\sigma^*$  is stress triaxiality given by  $\sigma^* = \sigma_m / \sigma_{\text{eq}}$ , and  $\sigma_m$  is mean stress. **Table 4** presents material model parameters taken from existing literature [68] for both steel types.



**Table 4.** Material model parameters for 304 stainless steel and 4340 steel.

Parameter	304 stainless steel [68]	4340 steel [69]
Density, $\rho$ ( $\text{kg}\cdot\text{m}^{-3}$ )	7800	7830
Young's modulus, $E$ (GPa)	200	200
Poisson's ratio, $\mu$	0.3	0.29
Static yield strength, $A$ (MPa)	310	792
Strain hardening constant, $B$ (MPa)	1000	510
Strain hardening exponent, $n$	0.65	0.26
Strain rate constant, $C$	0.07	0.014
Thermal softening exponent, $m$	1	1.03
Reference strain rate, $\dot{\epsilon}_0$ ( $\text{s}^{-1}$ )	1	1
Room temperature, $T_r$ ( $^{\circ}\text{C}$ )	293	293
Melting temperature, $T_m$ ( $^{\circ}\text{C}$ )	1673	1793
Specific heat, $C_r$ ( $\text{J}\cdot\text{kg}^{-1}\cdot\text{K}^{-1}$ )	440	477
Damage constant, $D_1$	0.6	0.05
Damage constant, $D_2$	0	3.44
Damage constant, $D_3$	0	-2.12
Damage constant, $D_4$	0	0.002
Damage constant, $D_5$	0	0.61

#### 4.2.2. Polyurea

To quantify the nonlinear and rate-sensitive response of Qtech-420 polyurea, the compressible visco-hyperelastic constitutive model proposed by the present authors in an earlier study [56] is adopted and numerically implemented into ABAQUS v2020 via a user-defined material (VUMAT) subroutine, with a Poisson ratio of 0.485 assumed for numerical reasons. For consistency, the theoretical framework detailed in [56] is briefly summarized below. For clarity, let the bold and italic characters represent the tensors and scalars, respectively. Upon the principle of stress decomposition, the Cauchy stress  $\boldsymbol{\sigma}^{\text{vh}}$  can be divided into two parts, i.e., a five-parameter

hyperelastic component  $\boldsymbol{\sigma}^{\text{he}}$  and a three-parameter viscoelastic component  $\boldsymbol{\sigma}^{\text{ve}}$ :

$$\boldsymbol{\sigma}^{\text{vh}} = \boldsymbol{\sigma}^{\text{he}} + \boldsymbol{\sigma}^{\text{ve}} \quad (6)$$

The rate-insensitive stress tensor  $\boldsymbol{\sigma}^{\text{he}}$  is calculated as:

$$\begin{aligned} \boldsymbol{\sigma}^{\text{he}} = & -2 \left( \left( A_2 + A_3 \left( J^{-\frac{2}{3}} I_1 - 3 \right) \right) J^{-\frac{7}{3}} \right) \mathbf{B}^2 \\ & + 2 \left( \left( A_1 + A_4 e^{-A_5 \left( J^{-\frac{2}{3}} I_1 - 3 \right)} \right) J^{-\frac{5}{3}} + \left( A_2 + A_3 \left( J^{-\frac{2}{3}} I_1 - 3 \right) \right) J^{-\frac{7}{3}} I_1 + A_3 \left( J^{-\frac{4}{3}} I_2 - 3 \right) J^{-\frac{5}{3}} \right) \mathbf{B} \\ & + \left( 2D(J-1) - \frac{2}{3} \left( A_1 + A_4 e^{-A_5 \left( J^{-\frac{2}{3}} I_1 - 3 \right)} \right) J^{-\frac{5}{3}} I_1 - \frac{4}{3} \left( A_2 + A_3 \left( J^{-\frac{2}{3}} I_1 - 3 \right) \right) J^{-\frac{7}{3}} I_2 - \frac{2}{3} A_3 \left( J^{-\frac{4}{3}} I_2 - 3 \right) J^{-\frac{5}{3}} \right) \mathbf{I} \end{aligned} \quad (7)$$

where  $\mathbf{B}$  is the left Cauchy-Green deformation tensor,  $\mathbf{I}$  is the unit tensor,  $I_1$  and  $I_2$  are the first two invariants of the right Cauchy-Green deformation tensor  $\mathbf{C}$ , and  $J$  is the Jacobian determinant of deformation gradient  $\mathbf{F}$ . On the other hand,  $\boldsymbol{\sigma}^{\text{ve}}$  is rate sensitive and can be written by:

$$\boldsymbol{\sigma}^{\text{ve}} = \frac{2(1+\mu)}{3(1-2\mu)} \left( G_\infty \boldsymbol{\varepsilon}_v + G_1 \int_0^t e^{-\frac{t-\tau}{\theta_1}} \dot{\boldsymbol{\varepsilon}}_v d\tau \right) \mathbf{I} + 2 \left( G_\infty \mathbf{s}^{\text{ve}} + G_1 \int_0^t e^{-\frac{t-\tau}{\theta_1}} \dot{\mathbf{s}}^{\text{ve}} d\tau \right) \quad (8)$$

where  $\boldsymbol{\varepsilon}_v$  and  $\mathbf{s}^{\text{ve}}$  are volumetric and deviatoric strains while  $\dot{\boldsymbol{\varepsilon}}_v$  and  $\dot{\mathbf{s}}^{\text{ve}}$  are volumetric and deviatoric strain rates.

Given that the model constants ( $A_1, A_2, A_3, A_4, A_5, G_\infty, G_1, \theta_1$ ) are commonly determined through quasi-static and dynamic uniaxial tests, the Cauchy stress tensor  $\boldsymbol{\sigma}^{\text{vh}}$  can be simplified to a one-dimensional (1D) form, as:

$$\begin{aligned} \sigma_{11} = & 2 \left( \frac{A_2}{\lambda^{2.01}} + \frac{A_1 + A_4 e^{-A_5 \left( -3 + \frac{2}{\lambda^{0.99} + \lambda^{1.98}} \right)}}{\lambda^{1.02}} \right) (-1 + \lambda^{2.97}) + \frac{6A_3 \left( -\lambda^{3.03} + \lambda^{4.02} + \lambda^{5.01} - \lambda^{6.99} - \lambda^{7.98} + \lambda^{8.97} \right)}{\lambda^{6.03}} \\ & + 2G_\infty \left( \lambda - \lambda^{-0.485} \right) + 2G_1 \int_0^t \left( 1 + 0.485 \lambda^{-1.485} \right) \dot{\lambda} e^{-\frac{t-\tau}{\theta_1}} d\tau \end{aligned} \quad (9)$$

where  $\sigma_{11}$  and  $\lambda$  are the Cauchy (true) stress and stretch in the loading direction, respectively. This theoretical model considers both compression and tension in the parameter evaluation process, which is beneficial for accurately capturing the inhomogeneous deformation of polyurea coating under complex stress states. **Figure 12** compares the measured and predicted mechanical response of polyurea at various strain rates, where positive and negative values of stretch rate denote tensile and compressive loading conditions. The optimal model constants are presented in **Table 5**. Moreover, fracture initiation of polyurea coating is determined using a simple criterion of maximum principal strain ( $\sim 0.5$ ).

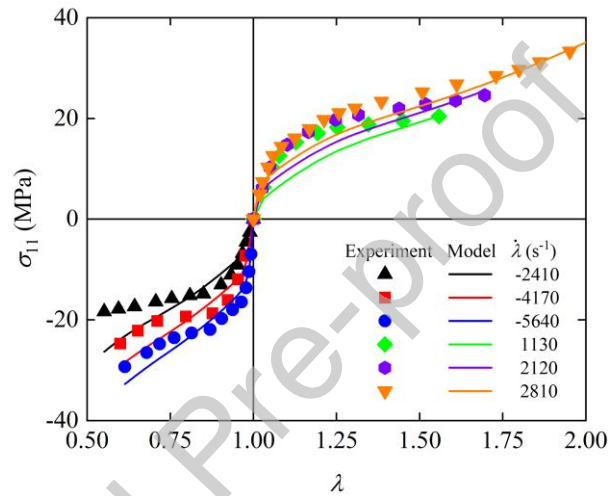


**Fig. 12.** Comparison between experimentally measured and numerically predicted true stress versus stretch curves of polyurea elastomer Qtech-420 at selected strain rates.

**Table 5.** Material model parameters for polyurea elastomer Qtech-420.

Parameters	Value
Density, $\rho$ ( $\text{kg}\cdot\text{m}^{-3}$ )	950
Young's modulus, $E$ (MPa)	30
Poisson ratio, $\mu$	0.485
Hyperelastic constant, $A_1$ (MPa)	1.107
Hyperelastic constant, $A_2$ (MPa)	0.231
Hyperelastic constant, $A_3$ (MPa)	0.0344
Hyperelastic constant, $A_4$ (MPa)	3.772
Hyperelastic constant, $A_5$	3.221

Viscoelastic constant, $G_\infty$ (MPa)	8.308
Viscoelastic constant, $G_1$ (MPa)	446.388
Viscoelastic constant, $\theta_1$ ( $\mu\text{s}$ )	1.658

#### 4.3. Numerical validation

First of all, energy conservation of each FE simulation should be checked for the reliability of simulation results. For this purpose, **Fig. 13** presents the numerically predicted energy versus time histories of non-coated specimen **S-6** and coated specimen **PS-4**, each experiencing the highest impact velocity in the respective group. It is testified that, at any time after projectile impact, the total energy of the whole system (with or without coating) remains almost constant. The hourglass energy (also named the artificial strain energy) is usually caused by excessive deformation and distortional of elements. According to the ABAQUS convention, a widely accepted tolerance is that the hourglass energy needs to be restricted to 10% of the total energy. The results of **Fig. 13** strictly meet this standard of energy balance, thereby indicating the prediction accuracy of the current FE models.

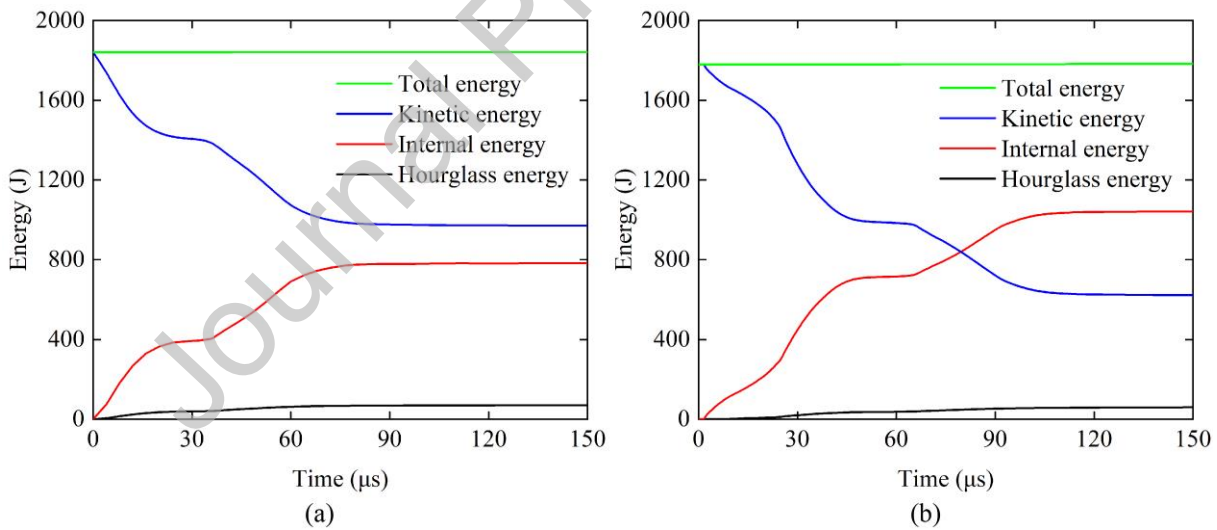


**Fig. 13.** Numerically predicted energy histories for (a) non-coated specimen **S-6** and (b) coated specimen **PS-4**.

**Figure 14** displays the internal energy evolutions of each substructure and projectile for **S-6** and **PS-4**, respectively. For the non-coated **S-6**, the absorbed energy of the rear face is much more than that of the impact face, the corrugate core, and the projectile (**Fig. 14a**), which is consistent with the results of Ni et al. [29]. By contrast, a 15 mm impact-side polyurea coating helps decelerate the projectile and contributes more to energy absorption of the coated **PS-4** than other substructures

(**Fig. 14b**). During the penetration of polyurea coating, the internal energy of the projectile varies slightly, indicating no evident projectile deformation/erosion in this process. More details about energy dissipation are presented in the discussion section that follows. Unless otherwise specified, the energy values reported in this work are obtained by multiplying the values extracted from the one-quarter FE models by 4.

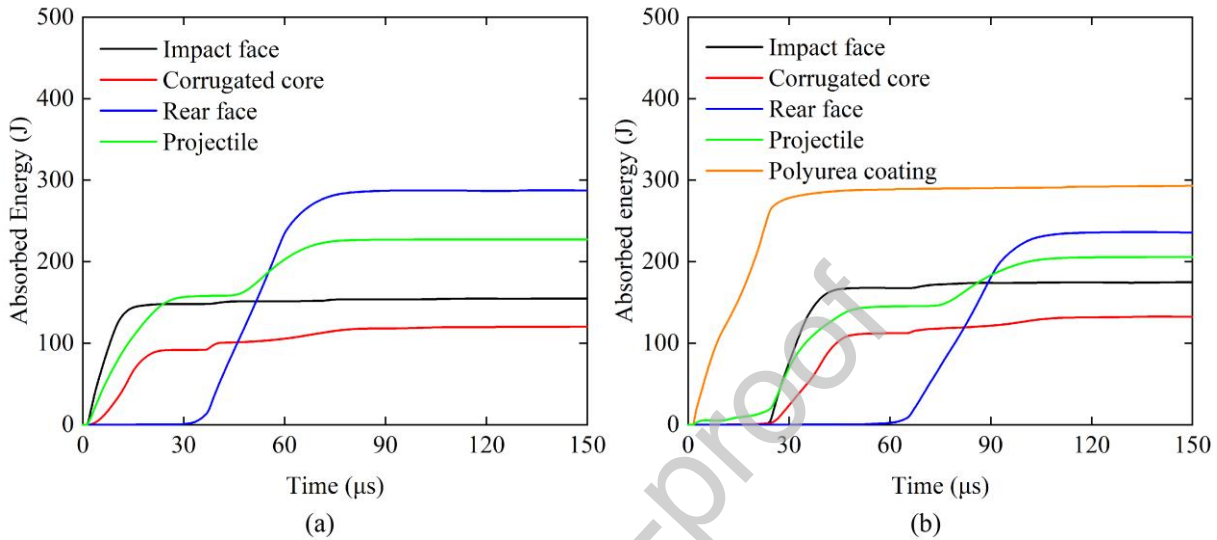


**Fig. 14.** Numerically predicted energy histories of each constituent for (a) S-6 and (b) PS-4.

The second step of numerical validation is to compare the measured and predicted ballistic resistance of both non-coated and coated samples. As depicted in **Fig. 15**, there is reasonable agreement between residual velocity versus impact velocity curves obtained from experiments and simulations. For the two types of samples investigated, the experimentally and numerically obtained ballistic limit velocities and perforation energy thresholds are approximately identical, with slight differences. The discrepancies may be attributed to two factors: (i) manufacturing defects in factual specimens are not considered in FE models; (ii) the face sheets and corrugated core are tied together in each specimen, with no debonding considered in FE simulation.

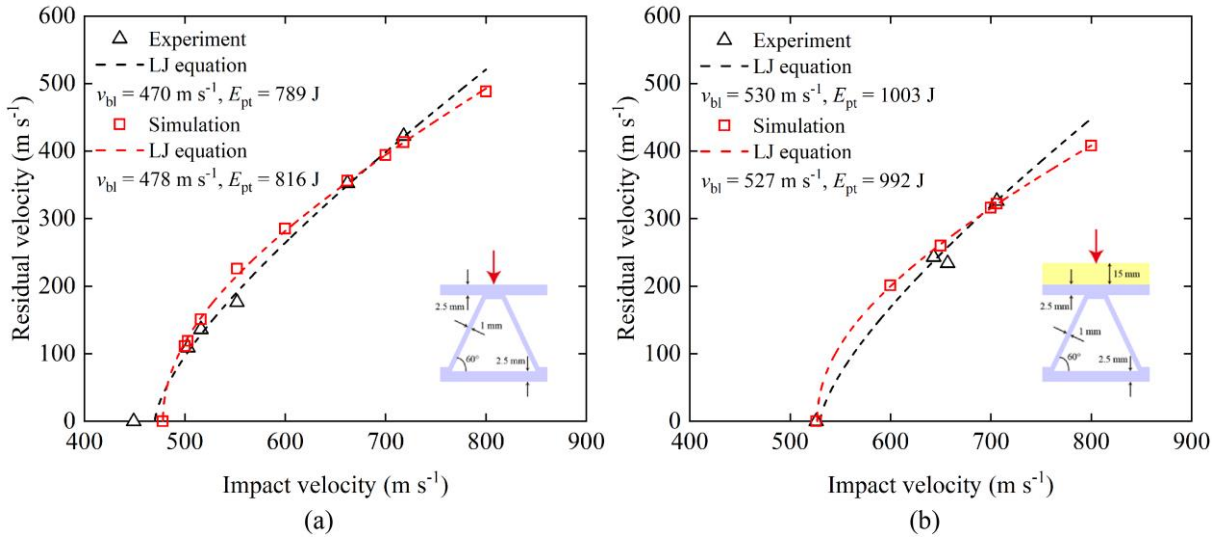


**Fig. 15.** Measured and predicted residual velocity versus impact velocity curves of (a) non-coated and (b) impact-side coated sandwich panels.

Next, how the projectile behaves in the entire penetration process is analyzed via FE simulations, with particular focus placed upon its velocity evolution. **Figure 16a** showcases the predicted projectile velocity history of non-coated **S-6** at an impact velocity of  $718 \text{ m}\cdot\text{s}^{-1}$ . To better describe the penetration process, the corresponding deformation and failure modes of the sandwich are presented in **Fig. 16b**, corresponding to Roman numerals “I ~ V” marked in **Fig. 16a**. The projectile velocity firstly undergoes a significant drop until point II, where both the impact face and core platform are entirely perforated, with plugging and joint fracture observed. Following a constant velocity period (points II ~ III), the partially eroded projectile is again decelerated, now by the rear face (points III ~ IV). As shown by the result corresponding to point V, the rear face is completely pierced with petalling and small debris observed.

Similarly, the velocity evolution and ballistic impact process of impact-side coated **PS-4** subjected to an impact velocity of  $706 \text{ m}\cdot\text{s}^{-1}$  are plotted in **Figs. 17a ~ b**. Similar to **S-6**, two significant velocity drops of the projectile are testified, i.e., points I ~ III and points IV ~ V. In addition to the failure modes of metallic substructures, the FE simulation also succeeds in describing the self-closing behaviour of polyurea coating after perforation: the hole size of polyurea coating recovers after penetration, becoming considerably smaller than projectile diameter, as shown by the result corresponding to point V. In a word, the current numerical method and material models are verified to be of high fidelity.

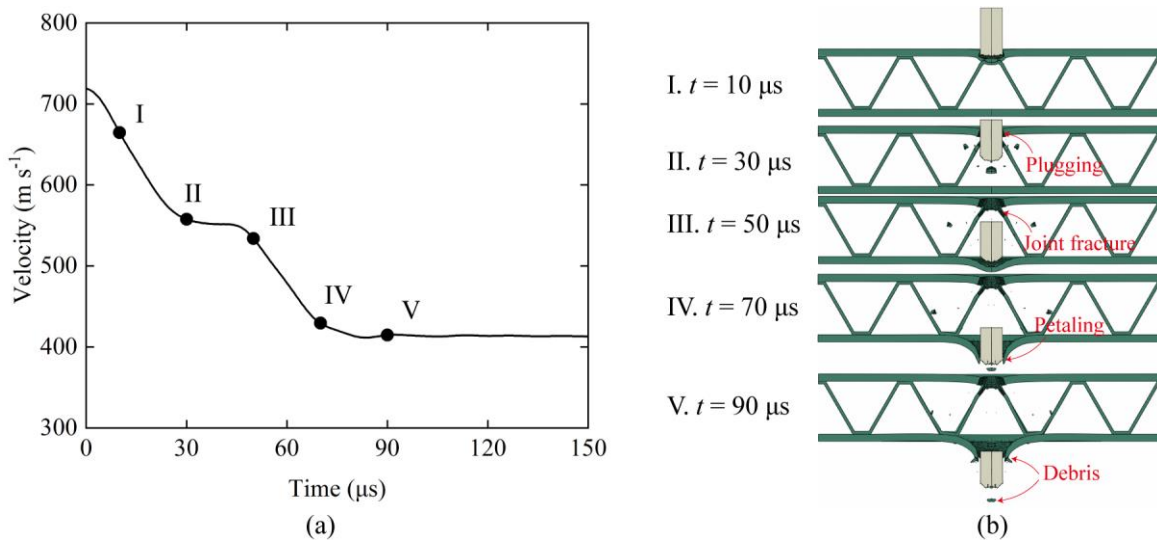


**Fig. 16.** Numerical results for non-coated specimen **S-6**: (a) projectile velocity history and (b) penetration process.

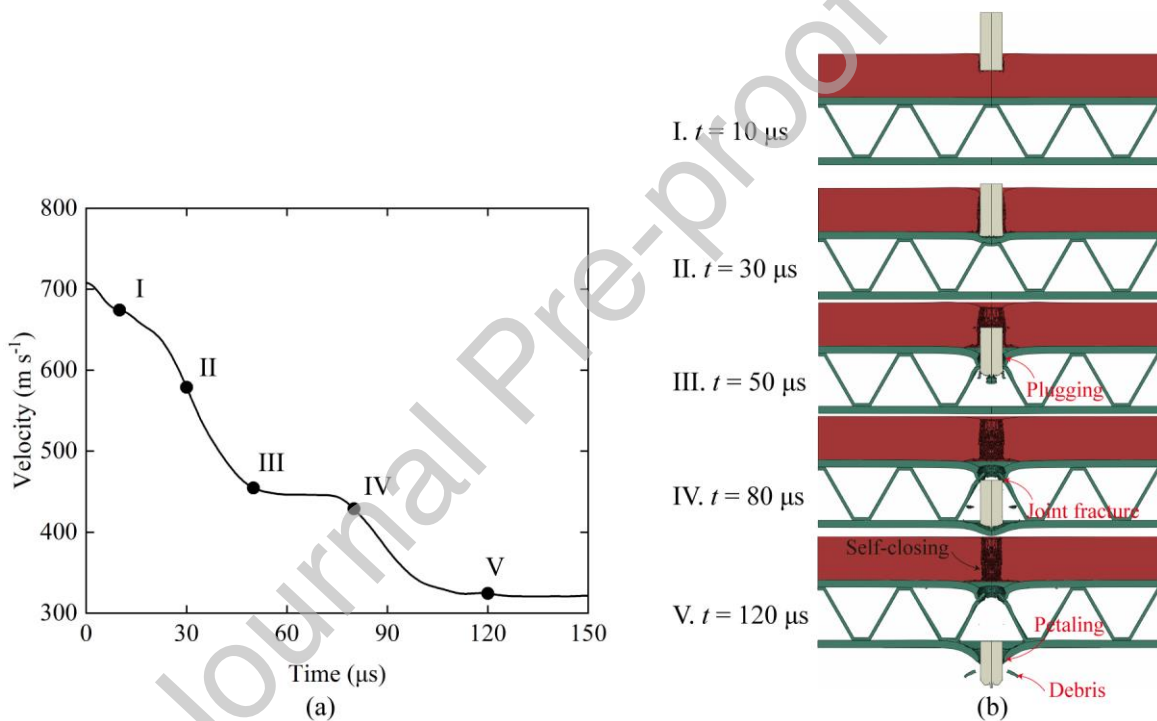


**Fig. 17.** Numerical results for impact-side coated specimen **PS-4**: (a) projectile velocity history and (b) penetration process.

#### 4.4. Discussion

Heretofore, the effects of impact-side polyurea coating on the ballistic impact response of metallic corrugated sandwich panels have been systematically disclosed, both experimentally and numerically. From the perspective of ballistic limit and energy absorption, one conclusion can be drawn - the front positioning of polyurea coating can effectively improve the penetration resistance

of corrugated sandwich panels against flat-ended projectile impact. For both non-coated and coated sandwich panels, good agreement is achieved between experimental measurements and numerical predictions on penetration process/failure modes/residual velocity curves. Next, based on the experimentally-validated FE model, four critical factors that may affect the ballistic limit and energy absorption characteristics are explored, i.e., coating position, coating thickness, projectile rigidity and projectile shape. The aim is to interrogate the protection mechanisms of elastomeric coating and optimize its mitigation effect on high-velocity ballistic impact.

#### 4.4.1. Coating position

First and foremost, how coating position on a corrugated sandwich panel affects its ballistic performance and energy dissipation is explored. Similar to the authors' previous studies [53,54], a coating thickness ratio is defined to quantify the distribution of impact-side and rear-side polyurea coating, with the total thickness of coating fixed so as to maintain the same weight of sandwich panels. Three different coating thickness ratios, 15/0, 7.5/7.5, and 0/15, are selected, and the total thickness of the coating is fixed at 15 mm. **Figure 18a** plots the residual velocity versus impact velocity curves of polyurea-coated sandwich panels with various coating thickness ratios. It is ascertained that better ballistic impact resistance is achieved via allocating more polyurea coating to the impact side. This finding is similar to the conclusion drawn from metal-polymer bilayer laminates [44–46,48]. Quantitatively, the existence of a 15 mm impact-side elastomeric coating raises the ballistic limit velocity by 10.3% (**Fig. 18b**) and the perforation energy threshold by 21.6% (**Fig. 18c**). Additionally, the energy absorption characteristics of non-coated and coated sandwich panels at three typical impact velocities are presented in **Fig. 19**, with particular focus on the role of polyurea coating. As shown in **Fig. 19a**, the impact-side coating is able to absorb much more energy than the rear-side and double-side ones. Typically, at an impact velocity of  $800 \text{ m}\cdot\text{s}^{-1}$ , the absorbed energy of the impact-side coating is 349 J, twice as much as that of the rear-side one. With the increase of incidence velocity, the energy dissipation undertaken by the impact-side coating is elevated from 238 to 349 J by 46.6%. To the authors' surprise, the impact-side coating accounts for more than 30% of the total energy absorption for the impact velocities considered, even superior to other metallic substructures of the corrugated sandwich, i.e., the face sheets and core (**Fig. 19b**).



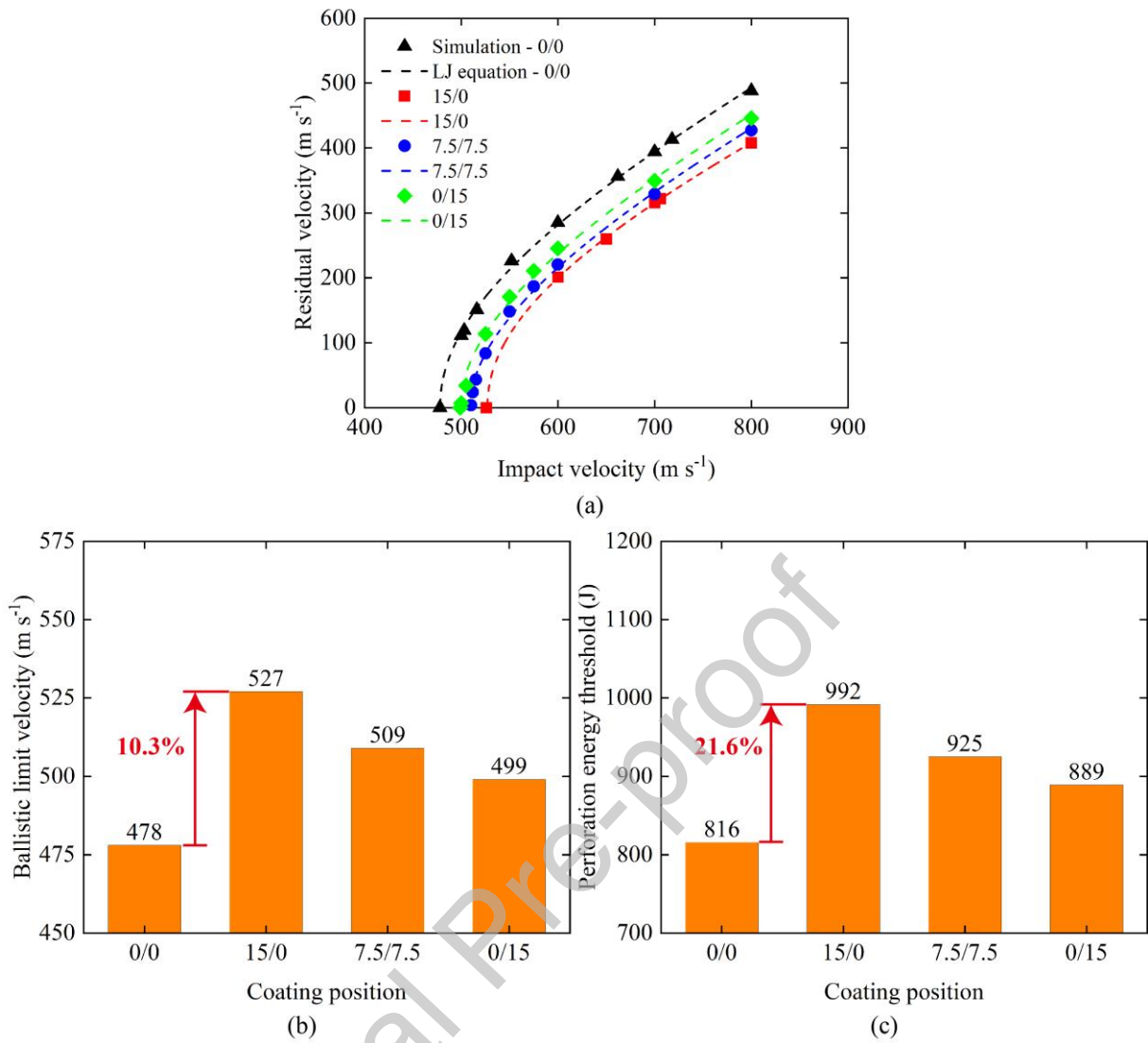


**Fig. 18.** Influence of coating position on (a) residual velocity versus impact velocity curve, (b) ballistic limit velocity, and (c) perforation energy threshold.

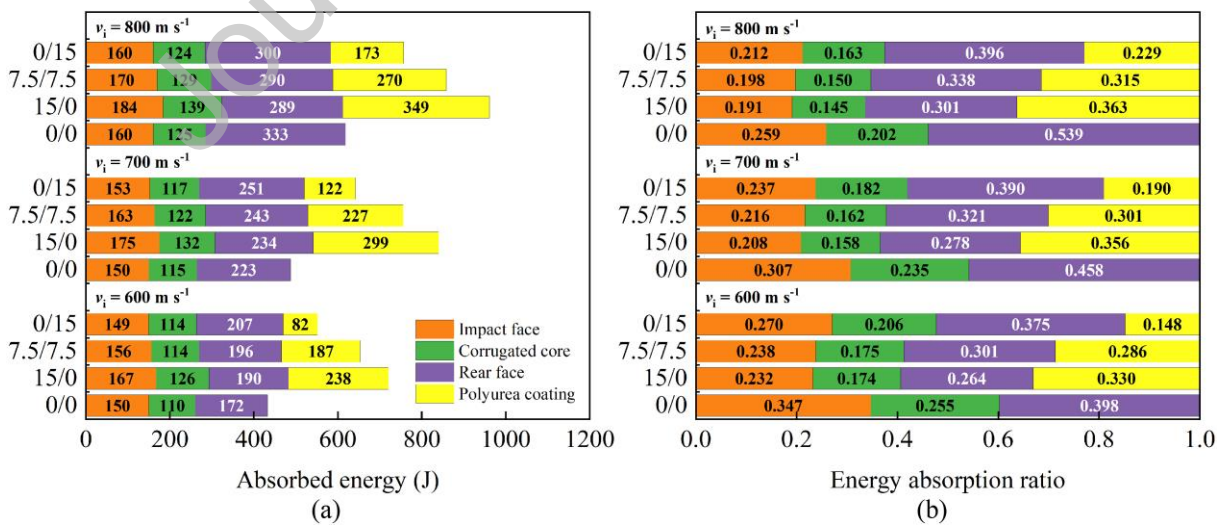


**Fig. 19.** Influence of coating position on (a) absorbed energy and (b) energy absorption ratio.

#### 4.4.2. Coating thickness

Next, the influence of coating thickness is quantified. Polyurea coating with varying thicknesses (i.e., 5, 10, 15, and 20 mm) is applied to the impact face. The residual velocity versus impact velocity curves of non-coated and coated sandwich panels are compared in **Fig. 20a**, while the corresponding ballistic limit velocities and perforation energy thresholds are presented in **Figs. 20b ~ c**. The results demonstrate that, with the elevation of coating thickness, the resistance of sandwich panels against ballistic impact is also enhanced. For instance, the presence of a 20 mm impact-side coating helps promote the ballistic limit velocity by 13.6% and the perforation energy threshold by 29.0%. Besides, the contribution of polyurea coating and other metallic substructures to energy absorption is summarized in **Fig. 21**. Consider the simulation results at the impact velocity of  $800 \text{ m}\cdot\text{s}^{-1}$ . With the coating thickness adjusted from 5 to 20 mm, the internal energy of elastomeric coating is significantly increased from 169 to 446 J by 163.9% (**Fig. 21a**). Accordingly, its energy absorption ratio is elevated from 21.7% to 43.7% by 101.4% (**Fig. 21b**). A similar benefit of polyurea reinforcing is observed as the impact velocity is varied. Of course, a thicker coating will sometimes lead to an undesirable increase in structural weight. As mentioned in **Fig. 17b**, the deformation area of polyurea coating is relatively narrow, so that the coating away from the crater is relatively useless. Therefore, to solve the trade-off between ballistic performance and structural weight, retrofitting the structure with a localized coating instead of a fully-coverage one is technically attractive.

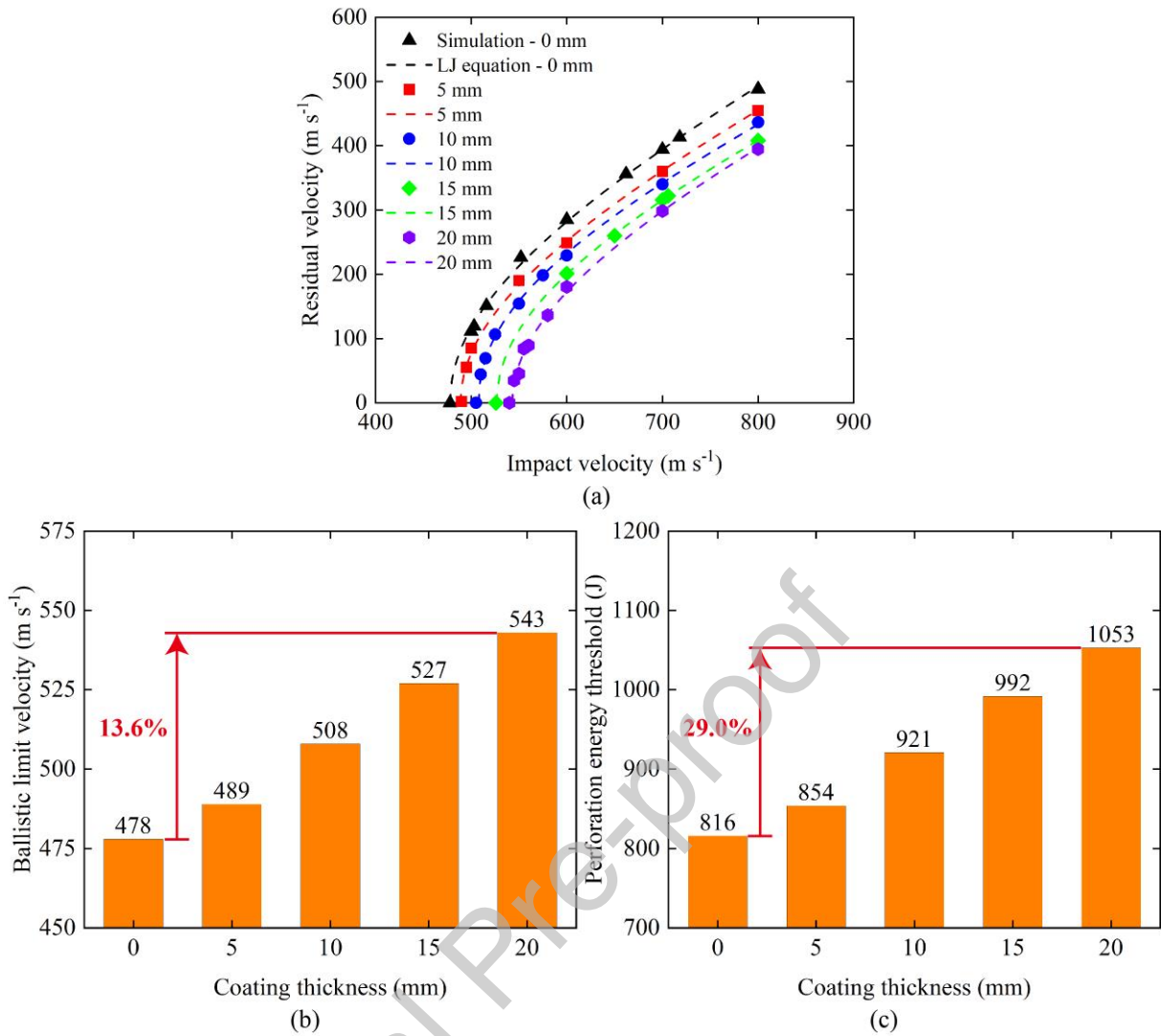


**Fig. 20.** Influence of coating thickness on (a) residual velocity versus impact velocity curve, (b) ballistic limit velocity, and (c) perforation energy threshold.

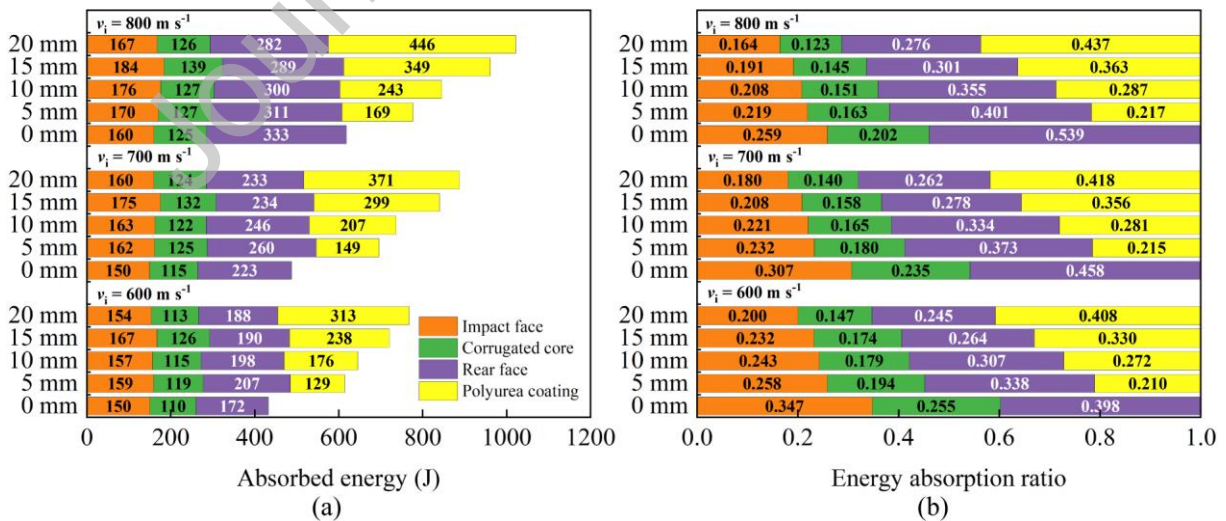


**Fig. 21.** Influence of coating thickness on (a) absorbed energy and (b) energy absorption ratio.

#### 4.4.3. Projectile rigidity

Thirdly, the effect of projectile rigidity on ballistic resistance is quantified. As mentioned earlier in **Fig. 14**, the kinetic energy of a projectile is partially dissipated by its own deformation and erosion. In practice, the projectiles may be made of different raw materials. So, to better evaluate the ballistic performance of a sandwich panel, the projectile is assumed to be rigid without any deformation or fracture. In this case, the impact energy should be entirely burdened by the sandwich, coated or non-coated. Recall the abbreviations of S for non-coated panels and PS for impact-side coated panels. For simplicity, let the deformable and rigid projectiles be denoted as DP and RP, respectively. A polyurea coating with a fixed thickness of 15 mm is applied to the impact face of each panel. **Figure 22** displays the residual velocity versus impact velocity curves of non-coated and impact-side coated panels, which are struck by both rigid and deformable projectiles. It is seen that the resistance of sandwich panels against rigid projectiles is weaker than that against deformable ones. Quantitatively, the ballistic limit velocity and perforation energy threshold of non-coated panels are curtailed from 478 to 345  $\text{m}\cdot\text{s}^{-1}$  (a drop of 27.8%) and from 816 to 425 J (a drop of 47.9%), respectively. Corresponding reductions for impact-side coated specimens are considerably less: 19.9% and 35.9%, respectively. However, an exciting finding should be noted that the effectiveness of polyurea coating in impeding rigid projectiles is superior. As shown in **Figs. 22b ~ c**, a 15 mm impact-side coating enhances the ballistic limit velocity by 22.3% and the perforation energy threshold by 49.6%. In terms of energy dissipation, there appears to be little difference in the energy absorbed by polyurea coating, whether the projectile is deformable or rigid (**Fig. 23a**). This is because only slight deformation and erosion occur in the deformable projectile during its penetration into the front-positioned polyurea layer. But, the role of polyurea coating in total energy absorption is more predominant when a rigid projectile strikes the panel (**Fig. 23b**).

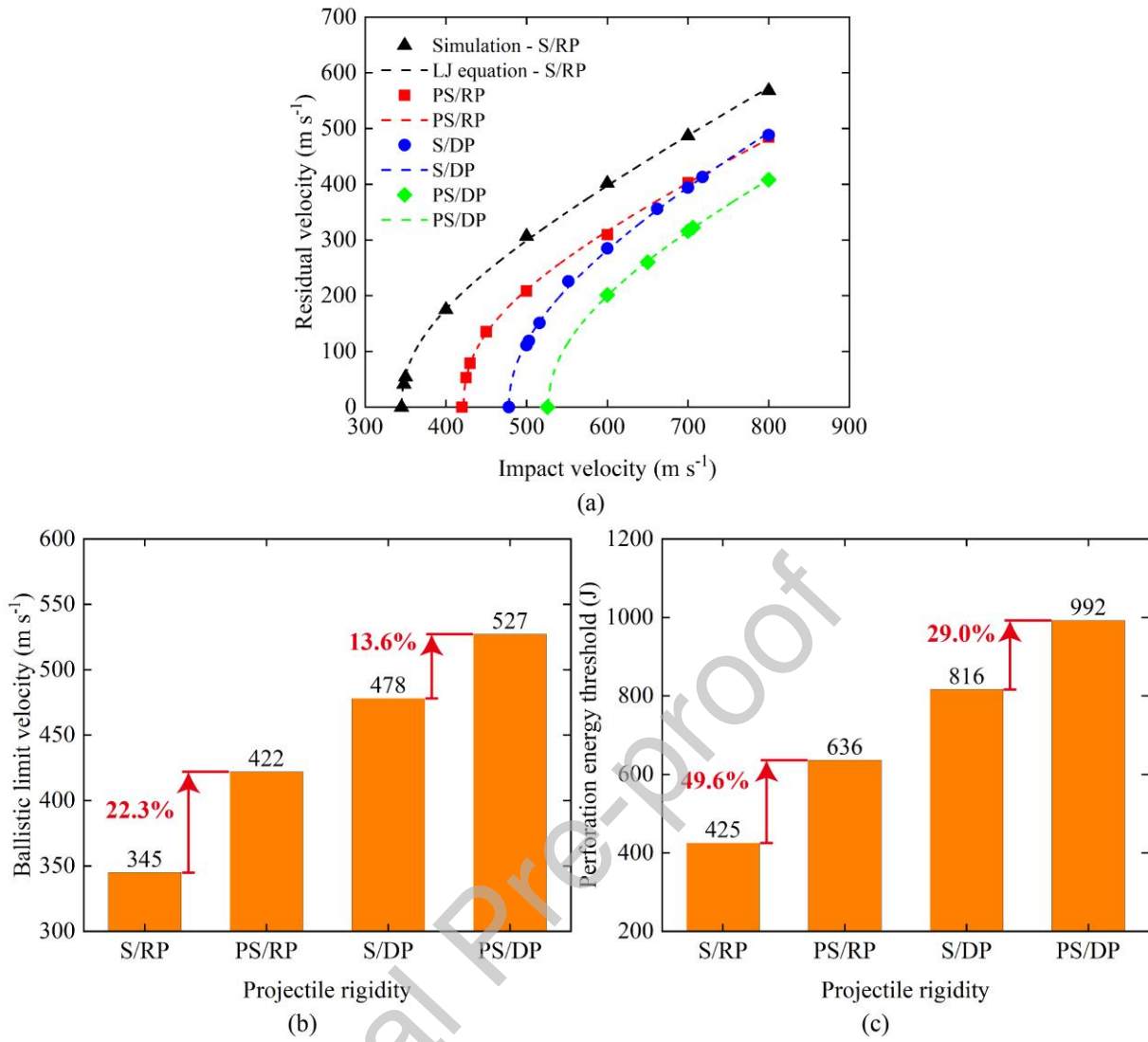


**Fig. 22.** Influence of projectile rigidity on (a) residual velocity versus impact velocity curve, (b) ballistic limit velocity, and (c) perforation energy threshold.

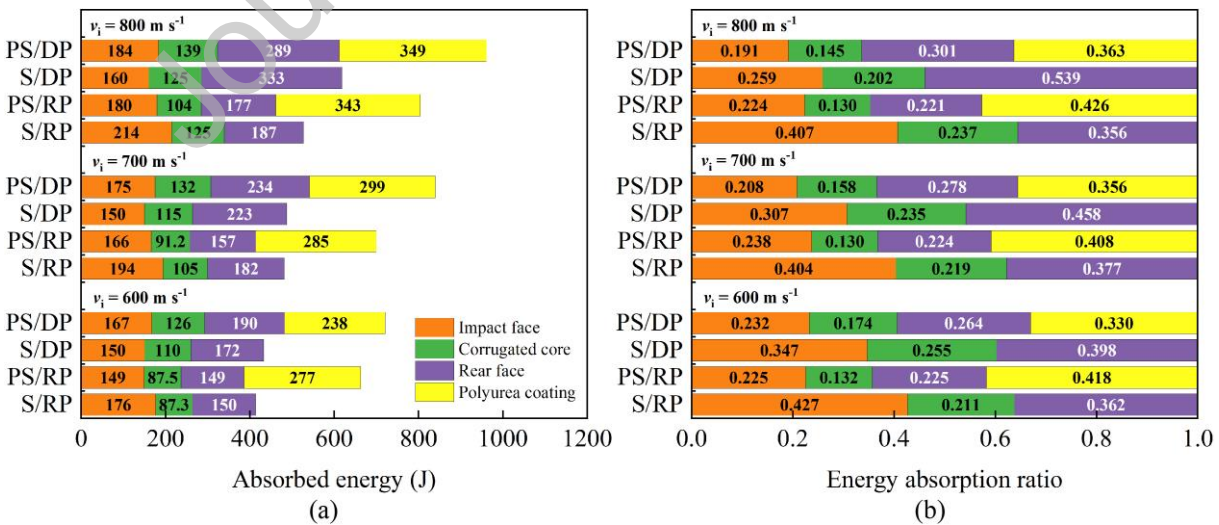


**Fig. 23.** Influence of projectile rigidity on (a) absorbed energy and (b) energy absorption ratio.

#### 4.4.4. Projectile shape

Upon the verified FE model, the dependence of projectile nose shape on the ballistic impact response of non-coated and coated panels is testified finally. The projectiles with three kinds of projectile nose shapes (i.e., flat-ended, conical, and hemispherical) are accepted for numerical simulation, with the detailed geometries shown in **Fig. 24**. For the same reason reported in **Section 4.4.3**, all of the projectiles are modelled as rigid bodies having a constant mass and diameter of 7.14 g and 7.62 mm. Recall the abbreviations of S for non-coated panels and PS for impact-side coated panels. For simplicity, let the flat-ended, conical, and hemispherical projectiles be denoted as F, C, and H, respectively. A polyurea coating with a fixed thickness of 15 mm is applied to the impact face of each panel. **Figures 25a ~ b** illustrate the residual velocity versus impact velocity curves of non-coated and impact-side coated panels. It is proved that the ballistic limits of both non-coated and coated samples against conical projectiles are the lowest, while those against flat-ended ones are the highest. As depicted in **Figs. 25c ~ d**, the ballistic impact mitigation of polyurea coating is closely related to the projectile nose shape, and the coating works worst at impeding the conical projectiles. Specifically speaking, only 10.0% and 21.0% improvement in the ballistic limit velocity and perforation energy threshold are realized in the case of conical projectiles. Similarly, under the joint impact of hemispherical projects, the coating enhances the quantitative parameters by 16.3% and 35.6%, respectively. Furthermore, the influence of projectile shape on penetration resistance can be understood through the energy absorption mechanism. As plotted in **Fig. 26**, the absorbed energy and energy absorption ratio of the coating pierced by conical projectiles are the lowest among the three impact loads of concern. Under this circumstance, the coating makes the smallest contribution to dissipating the projectile kinetic energy (independent of nose shape), thereby resulting in the most undesirable ballistic performance.



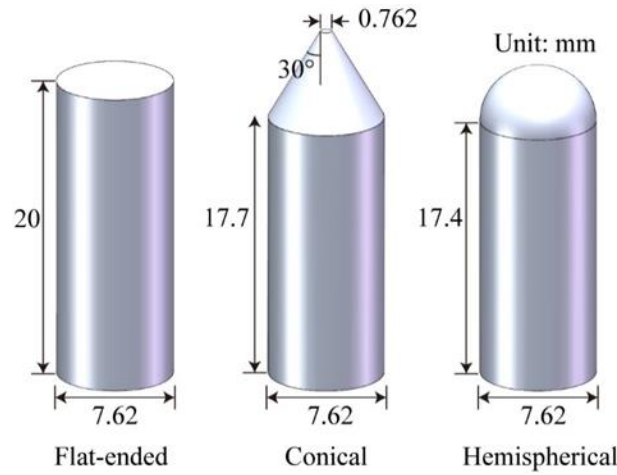


Fig. 24. Representative projectile nose shapes.

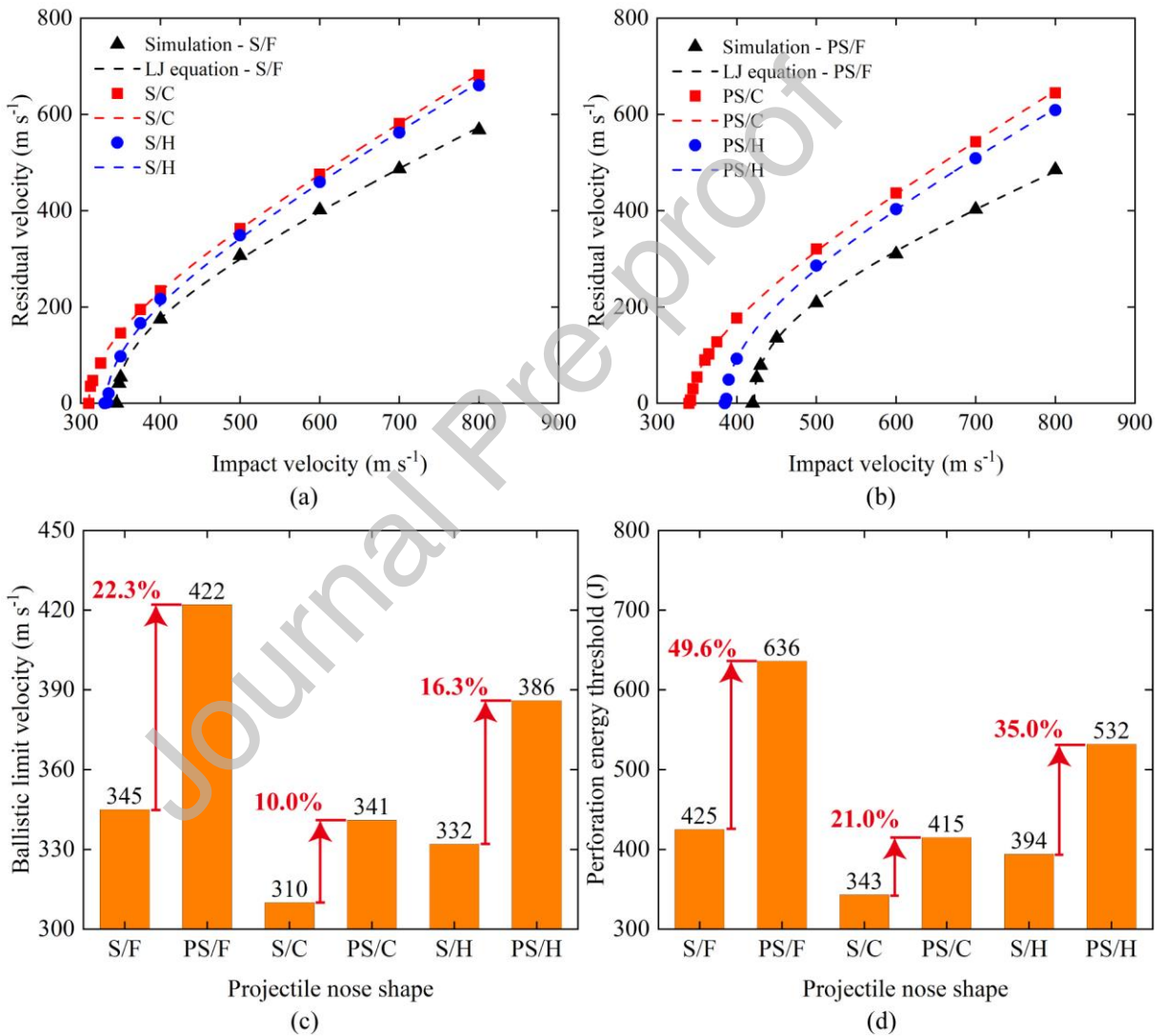


Fig. 25. Influence of projectile shape on (a, b) residual velocity versus impact velocity curve, (c) ballistic limit velocity, and (d) perforation energy threshold.

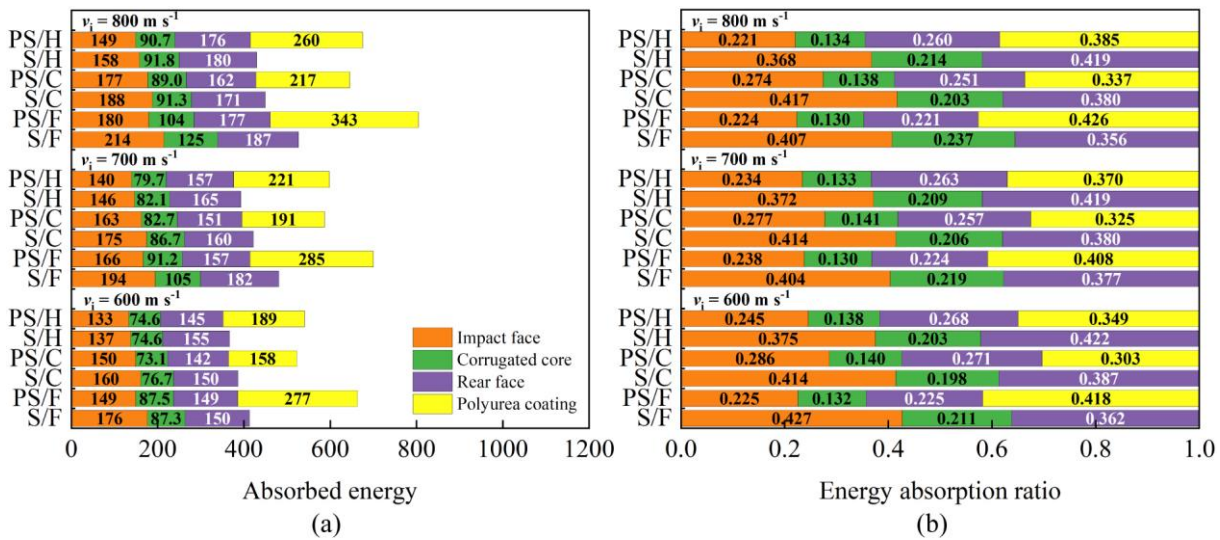


Fig. 26. Influence of projectile shape on (a) absorbed energy and (b) energy absorption ratio.

## 5. Concluding remarks

This study has carried out high-velocity impact tests in which flat-ended projectiles were used to penetrate both bare and elastomer-retrofitted metallic corrugated sandwich panels. In tandem with the experiments, FE calculations have also been undertaken to simulate the ballistic impact response of the sandwich panels studied. A summary of main findings is presented as follows:

(i) Using polyurea coating as a simple and viable technique to strengthen the ballistic resistance of all-metallic sandwich constructions is put forward for the first time. Experimental observations demonstrate that retrofitting a sandwich panel with a sufficiently thick (e.g., ~15 mm) impact-side coating provides a good elevation in its ballistic limit velocity and perforation energy threshold.

(ii) With the aid of a user-defined constitutive relation of polyurea coating, high-fidelity finite element (FE) simulation models of both non-coated and coated sandwich panels are established. There is excellent agreement between experimental and numerical results, including the residual velocity curves, ballistic limits, perforation energy thresholds, dynamic penetration process, and failure modes.

(iii) Upon the validated FE models, the effects of coating position and thickness on the ballistic performance of elastomer-retrofitted panels on ballistic performance are quantified. The use of a thicker and impact-side polyurea coating is able to absorb more impact energy of flat-ended projectiles, thereby better promoting ballistic resistance.



(iv) The benefit of polyurea coating is more evident in the resistance of sandwich construction to rigid, flat-ended projectiles rather than deformable, conical ones, due to a more predominant role of elastomeric coating in helping the sandwich to dissipate more impact energy of the former.

The current study provides useful insights for designing ultralightweight multifunctional sandwich constructions with enhanced ballistic impact resistance while maintaining their intrinsic structural attributes such as high specific stiffness/strength and energy absorption.

#### **Author statement**

**Xin Wang:** Conceptualization, Methodology, Software, Writing - Original Draft, Writing - Review & Editing.

**Zengshen Yue:** Investigation, Data curation.

**Haibo Ji:** Investigation, Validation.

**Zhongnan Zhao:** Investigation.

**Manyao Zhu:** Software.

**Xiang Xu:** Investigation.

**Pengfei Wang:** Investigation.

**Qiancheng Zhang:** Supervision, Writing - Review & Editing.

**Tian Jian Lu:** Supervision, Funding acquisition, Writing - Review & Editing.

#### **Conflict of interest statement**

The authors declare that they have no known competing financial interests or personal relationships that could have appeared to influence the work reported in this paper.

#### **Acknowledgements**

This work is supported by National Natural Science Foundation of China (11972185, 12072250, and 12002156). The first author thanks China Scholarship Council for a two-year scholarship (202006280483) and Prof. V.P.W. Shim for sharing the “3S” principle.

#### **Appendix. Influence of impact location on ballistic resistance**

The influence of impact location on the ballistic impact response of non-coated corrugated

core sandwich panels is numerically analyzed here. As illustrated in **Fig. A1a**, the sandwich panels are impacted at either a brazing joint of a corrugated core or mid-way between two joints. For clarity, these two loading conditions are denoted as joint impact and span impact, respectively. Upon the verified FE model, the predicted residual velocities are plotted in functions of impact velocities, as shown in **Fig. A1b**. It is proved that the ballistic limit of the non-coated panel under span impact ( $\sim 450 \text{ m}\cdot\text{s}^{-1}$ ) is about 5.8% lower than that under joint impact ( $\sim 478 \text{ m}\cdot\text{s}^{-1}$ ), indicating a slight influence of impact location. Besides, a similar topic was also experimentally figured out by Wadley et al. [35], and the results showed that the ballistic limit was approximately independent of impact location. Therefore, the authors believe the impact position more or less affects the ballistic resistance of corrugated sandwich construction, but the level of the influence might be associated with the geometries of structures and projectiles, material properties, and other factors. Note that only the joint impact is adopted for the present ballistic impact test.

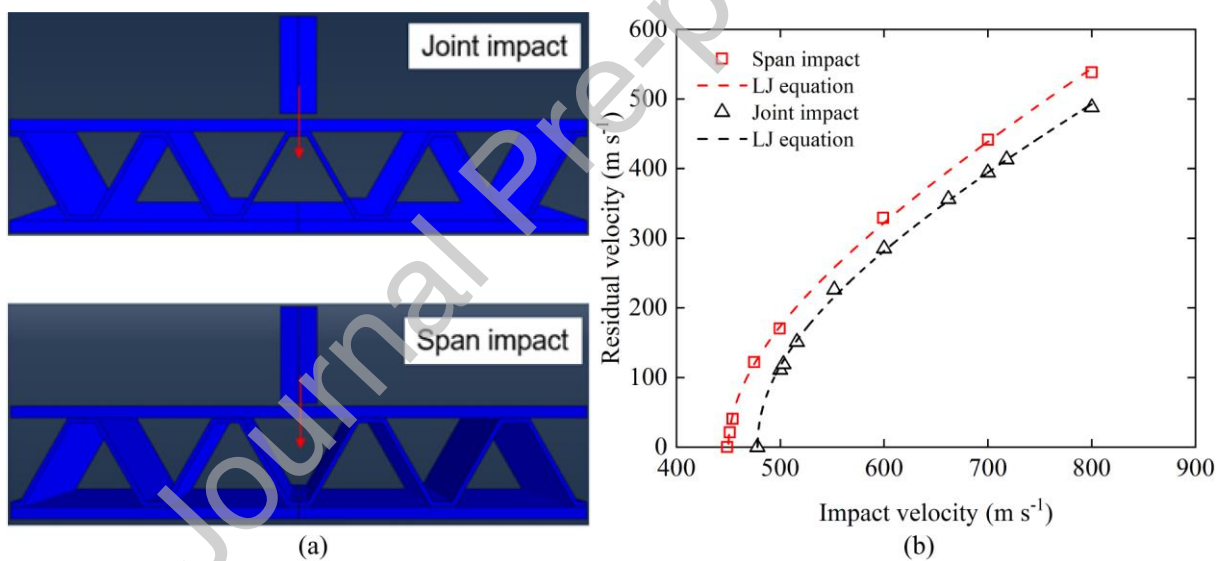


**Fig. A1.** Influence of impact location: (a) FE simulation models and (b) predicted residual velocity curves.

## References

- [1] Karasakal O, Özdemirel NE, Kandiller L. Anti-ship missile defense for a naval task group. *Nav Res Logist* 2011;58:304–21. <https://doi.org/10.1002/nav.20457>.
- [2] Yu R, Li X, Yue Z, Li A, Zhao Z, Wang X, et al. Stress state sensitivity for plastic flow and ductile fracture of L907A low-alloy marine steel: From tension to shear. *Mater Sci Eng A* 2022;835:142689. <https://doi.org/10.1016/j.msea.2022.142689>.
- [3] Li X, Yu R, Wang P, Kang R, Shu Z, Yue Z, et al. Plastic deformation and ductile fracture of L907A ship steel at increasing strain rate and temperature. *Int J Impact Eng* 2023:104515.

<https://doi.org/10.1016/j.ijimpeng.2023.104515>.

[4] Li Y, Ren X, Zhao T, Xiao D, Liu K, Fang D. Dynamic response of stiffened plate under internal blast: Experimental and numerical investigation. *Mar Struct* 2021;77.

<https://doi.org/10.1016/j.marstruc.2021.102957>.

[5] Jin J, Hou H, Chen P, Zhu X, Li D. Experimental study on the combined damage of liquid cabin structure subjected to charge explosion with preset fragments. *Int J Impact Eng* 2019;130:19–26. <https://doi.org/10.1016/j.ijimpeng.2019.04.001>.

[6] Kong XS, Wu WG, Li J, Chen P, Liu F. Experimental and numerical investigation on a multi-layer protective structure under the synergistic effect of blast and fragment loadings. *Int J Impact Eng* 2014;65:146–62. <https://doi.org/10.1016/j.ijimpeng.2013.11.009>.

[7] Zhang L, Du ZP, Gao P, Li Y. Research advance of damage load of surface ship cabin explosion (in Chinese). *Sci Sin Phys Mech Astron* 2021;51:124605.

<https://doi.org/10.1360/SSPMA-2020-0378>.

[8] Du ZP, Zhang XQ, Gao P, Li Y, Zhang L. Research on the mechanical characteristics of the Z-type target plate of the warhead entirely penetrating the ship simulation structure (in Chinese) 2021;51:124608. <https://doi.org/10.1360/SSPMA-2020-0360>.

[9] Grisaro HY, Dancygier AN. Characteristics of combined blast and fragments loading. *Int J Impact Eng* 2018;116:51–64. <https://doi.org/10.1016/j.ijimpeng.2018.02.004>.

[10] Kong X, Wu W, Li J, Liu F, Chen P, Li Y. A numerical investigation on explosive fragmentation of metal casing using Smoothed Particle Hydrodynamic method. *Mater Des* 2013;51:729–41. <https://doi.org/10.1016/j.matdes.2013.04.041>.

[11] Kang HJ, Choi J, Lee D, Park BJ. A framework for using computational fire simulations in the early phases of ship design. *Ocean Eng* 2017;129:335–42.

<https://doi.org/10.1016/j.oceaneng.2016.11.018>.

[12] Li L, Zhang Q, Zhang R, Xin W, Zhao Z, He S, et al. A laboratory experimental technique for simulating combined blast and impact loading. *Int J Impact Eng* 2019;134:103382.

<https://doi.org/10.1016/j.ijimpeng.2019.103382>.

[13] Paik JK. Innovative structural designs of tankers against ship collisions and grounding: A recent state-of-the-art review. *Mar Technol SNAME News* 2003;40:25–33.

<https://doi.org/10.5957/mt1.2003.40.1.25>.

[14] Frye D. Cuts Costs through Innovative Technology. *Adv Mater Process* 2011:21–5.

[15] Zhang P, Cheng Y, Liu J, Wang C, Hou H, Li Y. Experimental and numerical investigations on laser-welded corrugated-core sandwich panels subjected to air blast loading. *Mar Struct* 2015;40:225–46. <https://doi.org/10.1016/j.marstruc.2014.11.007>.

- [16] McShane GJ, Deshpande VS, Fleck NA. Underwater blast response of free-standing sandwich plates with metallic lattice cores. *Int J Impact Eng* 2010;37:1138–49. <https://doi.org/10.1016/j.ijimpeng.2010.05.004>.
- [17] Wadley HNG, Borvik T, Olovsson L, Wetzel JJ, Dharmasena KP, Hopperstad OS, et al. Deformation and fracture of impulsively loaded sandwich panels. *J Mech Phys Solids* 2013;61:674–99. <https://doi.org/10.1016/j.jmps.2012.07.007>.
- [18] Rubino V, Deshpande VS, Fleck NA. The dynamic response of end-clamped sandwich beams with a Y-frame or corrugated core. *Int J Impact Eng* 2008;35:829–44. <https://doi.org/10.1016/j.ijimpeng.2007.10.006>.
- [19] Wang H, Cheng Y, Liu J, Zhang P. Hydroelastic behaviours of laser-welded lightweight corrugated sandwich panels subjected to water impact: Experiments and simulations. *Thin-Walled Struct* 2020;146:106452. <https://doi.org/10.1016/j.tws.2019.106452>.
- [20] Huang W, Zhang W, Huang X, Jiang X, Li Y, Zhang L. Dynamic response of aluminum corrugated sandwich subjected to underwater impulsive loading: Experiment and numerical modeling. *Int J Impact Eng* 2017;109:78–91. <https://doi.org/10.1016/j.ijimpeng.2017.06.002>.
- [21] Li X, Wang Z, Zhu F, Wu G, Zhao L. Response of aluminium corrugated sandwich panels under air blast loadings: Experiment and numerical simulation. *Int J Impact Eng* 2014;65:79–88. <https://doi.org/10.1016/j.ijimpeng.2013.11.002>.
- [22] Rimoli JJ, Talamini B, Wetzel JJ, Dharmasena KP, Radovitzky R, Wadley HNG. Wet-sand impulse loading of metallic plates and corrugated core sandwich panels. *Int J Impact Eng* 2011;38:837–48. <https://doi.org/10.1016/j.ijimpeng.2011.05.010>.
- [23] Xu X, Zhang Y, Wang X, Fang J, Chen J, Li J. Searching superior crashworthiness performance by constructing variable thickness honeycombs with biomimetic cells. *Int J Mech Sci* 2022;235:107718. <https://doi.org/10.1016/j.ijmecsci.2022.107718>.
- [24] Yu R, Zhang Q, Wei Z, Li L, Yue Z, Wang X, et al. Dynamic response of fully-clamped steel plate under laboratory-simulated sequential fragment impact and blast loading. *Thin-Walled Struct* 2023;182:110144. <https://doi.org/10.1016/j.tws.2022.110144>.
- [25] Zhang P, Cheng Y, Liu J, Li Y, Zhang C, Hou H, et al. Experimental study on the dynamic response of foam-filled corrugated core sandwich panels subjected to air blast loading. *Compos Part B Eng* 2016;105:67–81. <https://doi.org/10.1016/j.compositesb.2016.08.038>.
- [26] Yue Z, Wang X, He C, Yu R, Li X, Zhao Z. Elevated shock resistance of all-metallic sandwich beams with honeycomb-supported corrugated cores. *Compos Part B Eng* 2022;242:110102. <https://doi.org/10.1016/j.compositesb.2022.110102>.
- [27] Yu R, Wang X, Zhang Q, Li L, He S, Han B, et al. Effects of sand filling on the dynamic

- response of corrugated core sandwich beams under foam projectile impact. *Compos Part B* 2020;197:108135. <https://doi.org/10.1016/j.compositesb.2020.108135>.
- [28] Wang X, Yu RP, Zhang QC, Li L, Li X, Zhao ZY, et al. Dynamic response of clamped sandwich beams with fluid-filled corrugated cores. *Int J Impact Eng* 2020;139:103533. <https://doi.org/10.1016/j.ijimpeng.2020.103533>.
- [29] Ni CY, Li YC, Xin FX, Jin F, Lu TJ. Ballistic resistance of hybrid-cored sandwich plates: Numerical and experimental assessment. *Compos Part A Appl Sci Manuf* 2013;46:69–79. <https://doi.org/10.1016/j.compositesa.2012.07.019>.
- [30] Ni C, Jin F, Lu T. Penetration of sandwich plates with hybrid-cores under oblique ballistic impact. *Theor Appl Mech Lett* 2014;4:021001. <https://doi.org/10.1063/2.1402101>.
- [31] Ni C, Hou R, Han B, Jin F, Ma G, Lu T. Normal and oblique projectile impact of double-layered pyramidal lattice truss structures filled with ceramic insertions. *J Thermoplast Compos Mater* 2017;30:1136–56. <https://doi.org/10.1177/0892705715618739>.
- [32] Khodaei M, Safarabadi Farahani M, Haghighi-Yazdi M. Numerical investigation of high velocity impact on foam-filled honeycomb structures including foam fracture model. *Mech Adv Mater Struct* 2020;0:1–13. <https://doi.org/10.1080/15376494.2020.1793239>.
- [33] Yungwirth CJ, Radford DD, Aronson M, Wadley HNG. Experiment assessment of the ballistic response of composite pyramidal lattice truss structures. *Compos Part B Eng* 2008;39:556–69. <https://doi.org/10.1016/j.compositesb.2007.02.029>.
- [34] Yungwirth CJ, Wadley HNG, O'Connor JH, Zakraysek AJ, Deshpande VS. Impact response of sandwich plates with a pyramidal lattice core. *Int J Impact Eng* 2008;35:920–36. <https://doi.org/10.1016/j.ijimpeng.2007.07.001>.
- [35] Wadley HNG, Dharmasena KP, O'Masta MR, Wetzel JJ. Impact response of aluminum corrugated core sandwich panels. *Int J Impact Eng* 2013;62:114–28. <https://doi.org/10.1016/j.ijimpeng.2013.06.005>.
- [36] Ni CY, Hou R, Xia HY, Zhang QC, Wang WB, Cheng ZH, et al. Perforation resistance of corrugated metallic sandwich plates filled with reactive powder concrete: Experiment and simulation. *Compos Struct* 2015;127:426–35. <https://doi.org/10.1016/j.compstruct.2015.02.059>.
- [37] Holmen JK, Børvik T, Hopperstad OS. Experiments and simulations of empty and sand-filled aluminum alloy panels subjected to ballistic impact. *Eng Struct* 2017;130:216–28. <https://doi.org/10.1016/j.engstruct.2016.09.057>.
- [38] Primeaux DJ. 100% solids aliphatic spray polyurea elastomer systems. *J Elastomers Plast* 1992;24:323–36.
- [39] Iqbal N, Tripathi M, Parthasarathy S, Kumar D, Roy PK. Polyurea coatings for enhanced

- blast-mitigation: A review. *RSC Adv* 2016;6:109706–17. <https://doi.org/10.1039/c6ra23866a>.
- [40] Amini M, Isaacs J, Nemat-Nasser S. Effect of polyurea on the dynamic response of steel plates. *Proc 2006 SEM Annu Conf Expo Exp Appl Mech Saint Louis (MO, United States) 2006*:1323–1326.
- [41] Amini MR, Isaacs JB, Nemat-Nasser S. Numerical modeling of response of monolithic and bilayer plates to impulsive loads. *Int J Impact Eng* 2010;37:82–9. <https://doi.org/10.1016/j.ijimpeng.2009.04.002>.
- [42] Amini MR, Isaacs JB, Nemat-Nasser S. Experimental investigation of response of monolithic and bilayer plates to impulsive loads. *Int J Impact Eng* 2010;37:82–9. <https://doi.org/10.1016/j.ijimpeng.2009.04.002>.
- [43] McShane GJ, Stewart C, Aronson MT, Wadley HNG, Fleck NA, Deshpande VS. Dynamic rupture of polymer-metal bilayer plates. *Int J Solids Struct* 2008;45:4407–26. <https://doi.org/10.1016/j.ijsolstr.2008.03.017>.
- [44] Roland CM, Fragiadakis D, Gamache RM. Elastomer-steel laminate armor. *Compos Struct* 2010;92:1059–64. <https://doi.org/10.1016/j.compstruct.2009.09.057>.
- [45] Gamache RM, Giller CB, Montella G, Fragiadakis D, Roland CM. Elastomer-metal laminate armor. *Mater Des* 2016;111:362–8. <https://doi.org/10.1016/j.matdes.2016.08.072>.
- [46] Roland CM, Fragiadakis D, Gamache RM, Casalini R. Factors influencing the ballistic impact resistance of elastomer-coated metal substrates. *Philos Mag* 2013;93:468–77. <https://doi.org/10.1080/14786435.2012.722235>.
- [47] Xue L, Mock W, Belytschko T. Penetration of DH-36 steel plates with and without polyurea coating. *Mech Mater* 2010;42:981–1003. <https://doi.org/10.1016/j.mechmat.2010.08.004>.
- [48] Zhang P, Wang Z, Zhao P, Zhang L, Jin XC, Xu Y. Experimental investigation on ballistic resistance of polyurea coated steel plates subjected to fragment impact. *Thin-Walled Struct* 2019;144:106342. <https://doi.org/10.1016/j.tws.2019.106342>.
- [49] Mohotti D, Ngo T, Mendis P, Raman SN. Polyurea coated composite aluminium plates subjected to high velocity projectile impact. *Mater Des* 2013;52:1–16. <https://doi.org/10.1016/j.matdes.2013.05.060>.
- [50] Chenwi IN, Ramotowski T, LeBlanc J, Shukla A. Effects of prolonged saline water exposure on the peel strength of polyurea/monel 400 interface. *J Adhes* 2021;00:1–17. <https://doi.org/10.1080/00218464.2021.1900829>.
- [51] Neba Mforsoh I, LeBlanc J, Shukla A. Constitutive compressive behavior of polyurea with exposure to aggressive marine environments. *Polym Test* 2020;85:106450. <https://doi.org/10.1016/j.polymertesting.2020.106450>.

- [52] Kim H, Citron J, Youssef G, Navarro A, Gupta V. Dynamic fracture energy of polyurea-bonded steel/E-glass composite joints. *Mech Mater* 2012;45:10–9. <https://doi.org/10.1016/j.mechmat.2011.08.017>.
- [53] Wang X, Li X, Yue ZS, Yu RP, Zhang QC, Du SF, et al. Optimal design of metallic corrugated sandwich panels with polyurea-metal laminate face sheets for simultaneous vibration attenuation and structural stiffness. *Compos Struct* 2021;256:112994. <https://doi.org/10.1016/j.compstruct.2020.112994>.
- [54] Wang X, Li X, Yu RP, Ren JW, Zhang QC, Zhao ZY, et al. Enhanced vibration and damping characteristics of corrugated sandwich panels with polyurea-metal laminate face sheets. *Compos Structures* 2020;251:112591. <https://doi.org/10.1016/j.compstruct.2020.112591>.
- [55] Wang X, He C, Yue Z, Li X, Yu R, Ji H, et al. Shock resistance of elastomer-strengthened metallic corrugated core sandwich panels. *Compos Part B Eng* 2022;237:109840. <https://doi.org/10.1016/j.compositesb.2022.109840>.
- [56] Wang X, Ji H, Li X, Sun S, Zhang Q, Shim VPW, et al. Static and dynamic compressive and tensile response of highly stretchable polyurea. *Int J Impact Eng* 2022;166:104250. <https://doi.org/10.1016/j.ijimpeng.2022.104250>.
- [57] Backman ME, Goldsmith W. The mechanics of penetration of projectiles into targets. *Int J Eng Sci* 1978;16:1–99. [https://doi.org/10.1016/0020-7225\(78\)90002-2](https://doi.org/10.1016/0020-7225(78)90002-2).
- [58] Yungwirth CJ, O'Connor J, Zakraysek A, Deshpande VS, Wadley HNG. Explorations of hybrid sandwich panel concepts for projectile impact mitigation. *J Am Ceram Soc* 2011;94:s62–75. <https://doi.org/10.1111/j.1551-2916.2011.04501.x>.
- [59] Cui T, Zhang J, Li K, Peng J, Chen H, Qin Q, et al. Ballistic limit of sandwich plates with a metal foam core. *J Appl Mech* 2021:1–51. <https://doi.org/10.1115/1.4052835>.
- [60] Zhou DW, Stronge WJ. Ballistic limit for oblique impact of thin sandwich panels and spaced plates. *Int J Impact Eng* 2008;35:1339–54. <https://doi.org/10.1016/j.ijimpeng.2007.08.004>.
- [61] Cai L, Al-Ostaz A, Li X, Fowler C, Cheng AHD, Alkhateb H. Protection of steel railcar tank containing liquid chlorine from high speed impact by using polyhedral oligomeric silsesquioxane-enhanced polyurea. *Int J Impact Eng* 2015;75:1–10. <https://doi.org/10.1016/j.ijimpeng.2014.06.015>.
- [62] Corbett GG, Reid ISR, Johnson W. FREE-FLYING PROJECTILES : A REVIEW 1996;18:141–230.
- [63] Hou W, Zhu F, Lu G, Fang DN. Ballistic impact experiments of metallic sandwich panels with aluminium foam core. *Int J Impact Eng* 2010;37:1045–55. <https://doi.org/10.1016/j.ijimpeng.2010.03.006>.

- [64] Ipson RFR and TW. Ballistic Perforation Dynamics. *J Appl Mech* 1963;30:384–91.
- [65] Lambert JP, Jonas GH. Towards standardization in terminal ballistics testing: velocity representation. 1976.
- [66] Fras T, Roth CC, Mohr D. Fracture of high-strength armor steel under impact loading. *Int J Impact Eng* 2018;111:147–64. <https://doi.org/10.1016/j.ijimpeng.2017.09.009>.
- [67] Fras T, Roth CC, Mohr D. Dynamic Perforation of Ultra-hard High-Strength Armor Steel: Impact Experiments and Modeling. *Int J Impact Eng* 2019;131:256–71. <https://doi.org/10.1016/j.ijimpeng.2019.05.008>.
- [68] Lee S, Barthelat F, Hutchinson JW, Espinosa HD. Dynamic failure of metallic pyramidal truss core materials - Experiments and modeling. *Int J Plast* 2006;22:2118–45. <https://doi.org/10.1016/j.ijplas.2006.02.006>.
- [69] Johnson GR, Cook WH. Fracture characteristics of three metals subjected to various strains, strain rates, temperatures and pressures. *Eng Fract Mech* 1985;21:31–48. [https://doi.org/10.1016/0013-7944\(85\)90052-9](https://doi.org/10.1016/0013-7944(85)90052-9).